Foundation punch-through in clay with sand: centrifuge modelling

S. N. ULLAH*, S. STANIER†, Y. HU† and D. WHITE‡

This paper is concerned with the vertical penetration resistance of conical spudcan and flat footings in layered soils. Centrifuge tests are reported for a clay bed with strength increasing with depth interbedded with dense and medium dense sand. Both non-visualising (full-model) and visualising (half-model) tests were conducted with high-quality digital images captured and analysed using the particle image velocimetry technique for the latter. The load–displacement curves often show a reduction in resistance on passing through the sand layers, which creates a risk of punch-through failure for the foundations when supporting a jack-up drilling unit. For a given foundation, the peak punch-through capacity (q_{peak}) is dependent on the thickness of both the overlying clay and the sand layer. The failure mechanism associated with the peak resistance in the sand layer involves entrapment of a thin band of top clay above the sand layer that subsequently shears along an inclined failure surface before being pushed into the underlying clay. The top clay height when normalised by the foundation diameter affects the soil failure pattern in this layer and along with the sand layer thickness controls the severity of the punch-through failure (i.e. the additional penetration before the resistance returns to the peak value). Comparisons are made with current industry guidelines for predicting q_{peak} and the risk of punch-through failure for sand overlying clay. These methods are shown to be conservative in their prediction of q_{peak} but inconsistent in predicting punch-through.

KEYWORDS: bearing capacity; centrifuge modelling; footings/foundations; model tests; offshore engineering; soil/structure interaction

INTRODUCTION

Jack-up rigs are commonly deployed in water depths of up to 150 m for extraction of hydrocarbons by drilling. The foundations of these jack-up rigs are penetrated into the seabed under water ballast preload to embed the foundations and improve their fixity prior to operation. During preloading punch-through can occur when a soft soil layer (such as soft clay) is overlain by a thin strong layer (such as dense sand or stiff clay) resulting in a rapid plunging of the foundation (e.g. Baglioni *et al.*, 1982). A comprehensive historical account (1957–2002) of jack-up foundation failures was given by Dier *et al.* (2004), and concluded that more than 50% of failures are associated with punch-through.

Punch-through has been the subject of extensive research in recent years. The soil stratigraphies that display the potential for punch-through include: (*a*) sand–clay stratigraphies (Teh *et al.*, 2010; Lee *et al.*, 2013a; Hu *et al.*, 2014a); (*b*) clay stratigraphies following a period of sustained preloading (Bienen & Cassidy, 2013; Stanier *et al.*, 2014; Bienen *et al.*, 2015); and (*c*) interbedded clay layers (Hossain *et al.*, 2011). Multi-layer deposits with interbedded sand are also common in regions with offshore hydrocarbon reserves, such as the Gulf of Suez, Southeast Asia, Gulf of Mexico and offshore South America (Baglioni *et al.*, 1982; Dutt &

Ingram, 1984; Teh *et al.*, 2009). Fig. 1 shows offshore borehole logs of clay stratigraphies with interbedded sand from the Gulf of Suez (Fig. 1(a)) and Gulf of Mexico (Fig. 1(b)) that could result in punch-through.

Research into the potential for punch-through at clay–sand–clay sites has been limited. Hossain (2014) recently reported a small number of experiments on clay–sand–clay stratigraphies. This paper reports two comprehensive sets of experiments – visualising (i.e. half-model particle image velocimetry (PIV) tests performed against a transparent window) and non-visualising (i.e. full-model penetration tests) – that were performed in a drum centrifuge. Both conical spudcan and flat foundation shapes were tested for a range of clay–sand–clay stratigraphy geometries (varying clay and sand layer heights) and a range of material properties (including sand relative density and clay shear strength). High-quality digital images captured during the visualising experiments have been analysed using the PIV technique (e.g. White *et al.*, 2003), allowing identification of the soil flow mechanisms at various key stages of the penetration process. Finally, the performance of the current industry guideline (SNAME, 2008; ISO, 2012) in predicting (*a*) the peak penetration resistance in the sand layer, (*b*) the bearing capacity in the underlying clay layer and (*c*) the maximum punch-through distance is assessed. The present paper reports the experimental findings; a companion paper develops an analytical model for prediction of the load–penetration response in sand–clay and clay–sand–clay stratigraphies (Ullah *et al.*, 2016a).

EXPERIMENTAL DETAILS
Centrifuge apparatus

The drum centrifuge at the University of Western Australia (UWA) (described by Stewart *et al.* (1998)) was used for all of the experiments reported. Visualising experiments were performed in strongboxes 180 mm (radial depth) by 258 mm (length) by 80 mm (width) in size, which were located and

* Department of Civil and Environmental Engineering, National University of Singapore, Singapore; formerly Centre for Offshore Foundation Systems, University of Western Australia, Crawley, WA, Australia.
† Centre for Offshore Foundation Systems, University of Western Australia, Crawley, WA, Australia.
‡ School of Civil, Resource and Mining Engineering, University of Western Australia, Crawley, WA, Australia.
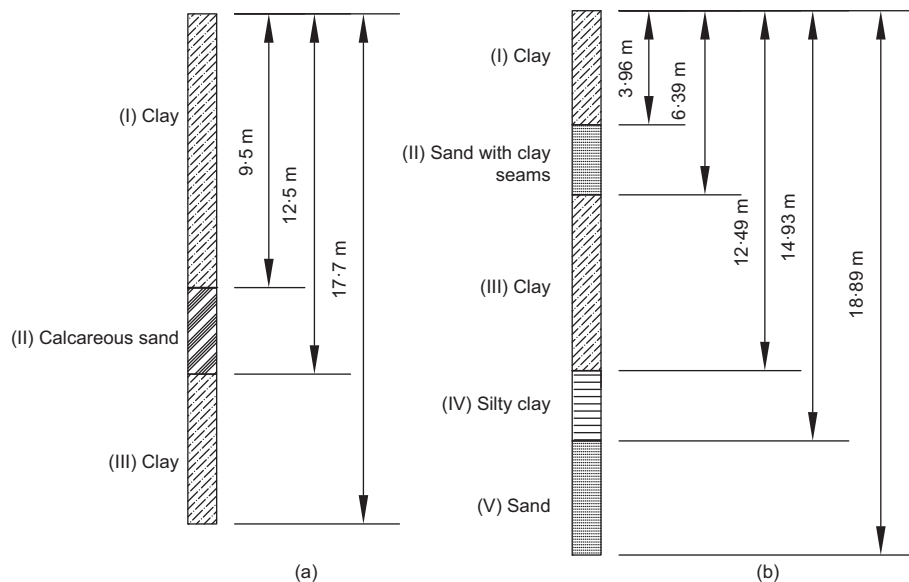
Fig. 1. Example of clay–sand–clay stratigraphies: (a) Gulf of Suez (after Dutt & Ingram, 1984); (b) Gulf of Mexico (after Baglioni et al., 1982)

observed within the centrifuge channel using the system described by Stanier & White (2013). Non-visualising experiments were performed within the drum centrifuge channel, which is 300 mm (width) by 200 mm (radial depth). All experiments were performed at an acceleration of 200g (where g is earth's gravitational acceleration).

Soil sample preparation

Commercially available kaolin clay powder and superfine silica sand were used in all of the experiments. The relevant engineering properties are reported by Lee *et al.* (2013a). Particle size distributions can be found for these two materials in Xu (2007). The soil samples were created using a multi-stage process. First, clay slurry was mixed to approximately twice its liquid limit and poured into the drum centrifuge strongbox or channel (for visualising and non-visualising tests, respectively) in-flight, at an acceleration of 20g. The clay was subsequently consolidated at 300g with periodic top-ups of further slurry, resulting in a bed of normally consolidated clay ~170 mm deep in the case of the non-visualising tests and ~140 mm in the visualising tests. The upper layer of clay was removed from the sample, leaving approximately 80 mm and 120 mm of clay in the strongboxes and centrifuge channel, respectively.

For the visualising experiments performed in the strongbox, sand was pluviated into the strongbox at 1g. The sand layer was scraped flat to achieve the desired sand layer height, and then a part of the clay layer previously removed was placed back to achieve the desired clay layer height. To provide additional image texture for the PIV analyses, coloured modelling flock was sprinkled uniformly onto the exposed plane of the model using a sieve after careful removal of the transparent window. The density of this modelling flock was optimised by matching it to that identified for the optimal artificial seeding ratio (ASR) following the procedure proposed by Stanier & White (2013). Different coloured modelling flock was used for the sand and clay layers to distinguish them in the images captured.

For the non-visualising full drum channel experiments superfine silica sand was air-pluviated in-flight through a layer of surface water in the channel onto a porous fabric filter placed on top of the clay sample. The pluviation nozzle and sand particle falling height were controlled to achieve the desired relative density (I_D) of the sand layer (i.e. larger nozzles and lower fall heights led to looser sand layers). The sample was spun for a further period at 200g to allow the sand layer to settle and the underlying clay layer to consolidate further. Cracking in the surface of the sand layer was observed due to the increase in circumference of the sand surface caused by its settlement in the channel. Thus, after the completion of consolidation, the original sand layer and porous fabric filter were removed and a new sand layer was pluviated into the channel directly onto the consolidated clay. The sand surface was then scraped radially using a thin aluminium sheet to achieve the first target sand layer height. After this, an overlying clay layer was created by pouring more clay slurry into the centrifuge channel in-flight for the non-visualising experiments. Following consolidation of the top clay layer, the sample surface was scraped to achieve the initial target overlying clay layer height.

Experimental procedure

All foundation penetration tests were performed at a penetration velocity v such that the dimensionless penetration rate V ($= vD/c_v$; where D is the foundation diameter and c_v is the coefficient of consolidation of the clay, which was taken as 2 m²/year) was 120 (the respective penetration velocity for each test is given in Table 2). This ensured undrained penetration through the clay layers and drained penetration in the sand layer (Lee *et al.*, 2013a). In all cases the foundation was penetrated into the sample until it was within one diameter of the base of the centrifuge strongbox or channel. To minimise the influence of disturbances caused by prior tests, the smaller foundations were tested first in the drum centrifuge channel followed by the larger foundations. Fifteen tests spaced at a minimum of 3D centre-to-centre were performed in the drum centrifuge channel and two tests were performed on opposing sides of each strongbox with a minimum spacing of ~2·7D (centre-to-centre). The potential boundary effects (bottom and sidewall) were assessed to be negligible at the final penetration depth using expressions and design charts derived from a database of large-deformation numerical analyses reported in Ullah *et al.* (2014) and Ullah *et al.* (2016b). The penetration force was measured during the penetration using a load cell at the top of the shaft of the foundation.

During the visualising experiments, high-resolution images of the exposed plane of the model were captured using the system described by Stanier & White (2013). In brief, the camera used was a 5 megapixel Prosilica GC2450C machine vision camera coupled with a Goya C-Mount 8 mm focal length lens. Illumination of the model was provided by two large light-emitting diode (LED) panels located above and below the field of view (FOV). Diffusing lenses were used to minimise glare in the images captured. Images were captured and downloaded, in-flight, in real time using a Gigabit Ethernet link passed across a fibre-optic rotary joint at a rate of 5 Hz throughout the penetration tests. The image capture times were synchronised with the actuator position, enabling direct correlation of the image and foundation position.

At the end of testing, the half foundation models used in the visualising experiments were placed against the transparent window and penetrated into water to calibrate for buoyancy and potential window friction. Similar buoyancy calibrations were also performed for the full drum channel non-visualising experiments.

Model geometries

The geometry of each layered model is described throughout as ratio of the layer heights (H_{ct} and H_s) to the foundation diameter (D) (Fig. 2(a)). A wide range of $H_{ct}/D = 0$–1.07 and $H_s/D = 0.25$–1.04 ratios was modelled, covering the range of practical interest (punch-through has not been reported for $H_s/D > 1$ (Hu et al., 2014a)). The spudcan and flat foundation geometries are illustrated in

Figs 2(b) and 2(c) and the sizes are summarised in Table 1. The spudcan had a shallow base inclination of 13° with a 76° protruding spigot, resembling the Marathon LeTourneau design class (SDC 82) widely used to support jack-up structures offshore. The flat foundations used in the non-visualising experiments performed in the drum centrifuge channel had a radiused underside matching the distance from the centre of rotation of the drum centrifuge to the clay surface. This improved the initial contact of the flat foundations with the sample on touchdown (Lee et al., 2013a).

To maximise the range of normalised geometries and facilitate cross comparisons, the drum centrifuge channel was divided into three sections (sections a, b and c). Section a had the maximum sand height. Following completion of the tests planned within section a, the upper clay was removed, allowing the sand layer to be scraped further to achieve a thinner sand layer before a layer of clay was consolidated on top. This process was repeated for sections b and c to model a wide range of normalised geometries.

Soil properties

The soil properties for each experiment are listed in Table 2, using the notation shown on Fig. 2(a). The relative density (I_D) and effective unit weight of the sand (γ'_s) were estimated using the maximum and minimum void ratios (e_{max} and e_{min}) reported by Lee et al. (2013a) for superfine silica sand in two different ways. For the visualising experiments performed in strongboxes, the sand pluviation apparatus was carefully calibrated to create samples of a
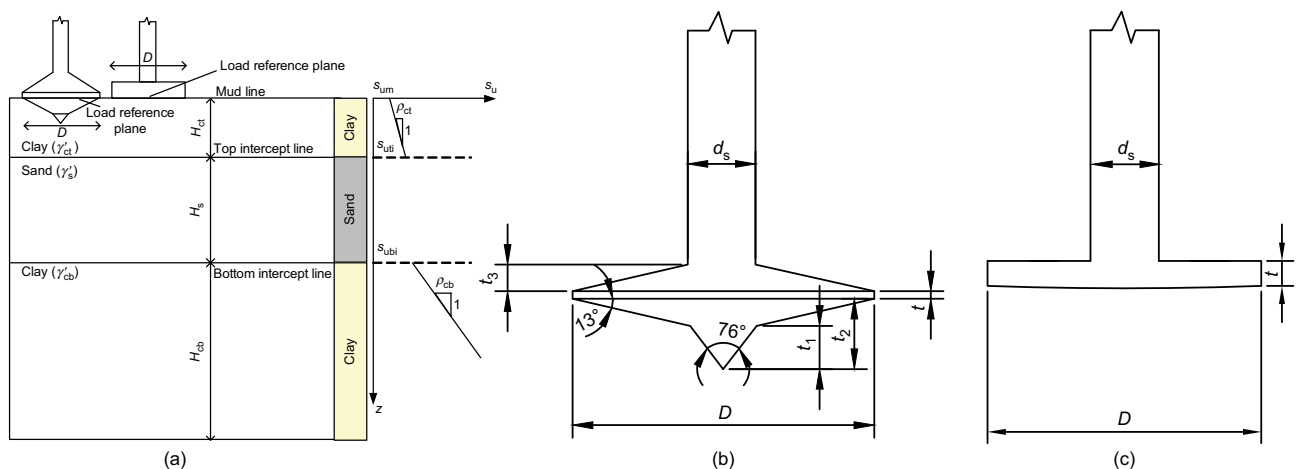

Fig. 2. Soil layers and foundation geometries: (a) three-layer clay–sand–clay stratigraphy; (b) spudcan foundation; (c) flat-based foundation

Table 1. Foundation prototype geometries at 200g

Type of foundation	D*: m	d_s*: m	t_1*: m	t_2*: m	t_3*: m	t: m
Spudcan (visualising)	6	1.35	0.86	1.40	0.35	0.15
Flat (visualising)	6	1.35	—	—	—	1.0
Spudcan (non-visualising)	6	2.92	0.86	1.40	0.35	0.30
	8	2.92	1.15	1.87	0.58	0.30
	10	2.92	1.44	2.33	0.81	0.30
	12	2.92	1.44	2.80	1.07	0.30
	14	2.92	2.02	3.27	1.27	0.30
	16	2.92	2.30	3.73	1.50	0.30
Flat (non-visualising): Cylindrical curvature	6	2.92	—	—	—	0.55
on underside of 420 mm radius	12	2.92	—	—	—	1.19
	16	2.92	—	—	—	1.42

*The geometric parameters D, d_s, t_1, t_2 and t_3 are defined in Fig. 2.

Table 2. Details of test geometries and soil properties (all tests conducted at 200g)

Test*	H_{ct}: m	H_s: m	D: m	H_{ct}/D: -	H_s/D: -	s_{um}: kPa	ρ_{ct}: kPa/m	s_{ubi}: kPa	ρ_{cb}: kPa/m	φ_{cv}: deg	I_D: %	γ'_s: kN/m³	γ'_{ct}†: kN/m³	γ'_{cb}†: kN/m³	v: mm/s	Remarks
T1SP	2·38	4	6	0·40	0·67	4·9	1·9	25·6	2·5	31	74	10·6	6·85	7·32	0·254	PIV visualising tests
T2SP	4·32	4	6	0·72	0·67	4·5	1·6	27	2·5	31	74	10·6	6·85	7·32	0·254	
T3SP	5·47	4	6	0·91	0·67	4·1	1·5	26	2·3	31	74	10·6	6·85	7·32	0·254	
T4SP	0	4	6	0·00	0·67	0	0	18·7	2	31	74	10·6	6·85	7·32	0·254	
T5SP	3·44	2	6	0·57	0·33	4·7	1·7	18·2	2	31	74	10·6	6·85	7·32	0·254	
T6SP	4·35	6	6	0·72	1·00	4·5	1·6	26	2·3	31	74	10·6	6·85	7·32	0·254	
T1FL	2·35	4	6	0·39	0·67	4·9	1·9	25·6	2·5	31	74	10·6	6·85	7·32	0·254	
T2FL	4·01	4	6	0·67	0·67	4·5	1·6	26·7	2·5	31	74	10·6	6·85	7·32	0·254	
T3FL	5·10	4	6	0·85	0·67	4·1	1·5	25·8	2·3	31	74	10·6	6·85	7·32	0·254	
T4FL	0	4	6	0·00	0·67	0	0	18·7	2	31	74	10·6	6·85	7·32	0·254	
T5FL	3·36	2	6	0·56	0·33	4·8	1·7	18·1	2	31	74	10·6	6·85	7·32	0·254	
T6FL	4·05	6	6	0·68	1·00	4·5	1·6	26	2·3	31	74	10·6	6·85	7·32	0·254	
SPa16	6·42	6·25	16	0·40	0·39	0·2	0·5	22·6	2·2	31	51	10·14	6·61	7·63	0·095	Full drum tests: section a
SPa14	6·42	6·25	14	0·46	0·45	0·2	0·5	22·6	2·2	31	51	10·14	6·61	7·63	0·109	
SPa12	6·42	6·25	12	0·54	0·52	0·2	0·5	22·6	2·2	31	51	10·14	6·61	7·63	0·127	
SPa10	6·42	6·25	10	0·64	0·63	0·2	0·5	22·6	2·2	31	51	10·14	6·61	7·63	0·152	
SPa6	6·42	6·25	6	1·07	1·04	0·2	0·5	22·6	2·2	31	51	10·14	6·61	7·63	0·254	
FLa6	6·42	6·25	6	1·07	1·04	0·2	0·5	22·6	2·2	31	51	10·14	6·61	7·63	0·254	
SPb16	6·32	4	16	0·39	0·25	0·2	0·5	24·6	2·4	31	51	10·14	6·61	7·63	0·095	Full drum tests: section b
SPb12	6·32	4	12	0·53	0·33	0·2	0·5	24·6	2·4	31	51	10·14	6·61	7·63	0·127	
SPb8	6·32	4	8	0·79	0·50	0·2	0·5	24·6	2·4	31	51	10·14	6·61	7·63	0·190	
SPb6	6·32	4	6	1·05	0·67	0·2	0·5	24·6	2·4	31	51	10·14	6·61	7·63	0·254	
FLb12	6·32	4	12	0·53	0·33	0·2	0·5	24·6	2·4	31	51	10·14	6·61	7·63	0·127	
SPc16	4	4	16	0·25	0·25	0·3	0·58	23	2·5	31	51	10·14	6·61	7·63	0·095	Full drum tests: section c
SPc8	4	4	8	0·50	0·50	0·3	0·58	23	2·5	31	51	10·14	6·61	7·63	0·190	
SPc6	4	4	6	0·67	0·67	0·3	0·58	23	2·5	31	51	10·14	6·61	7·63	0·254	
FLc16	4	4	16	0·25	0·25	0·3	0·58	23	2·5	31	51	10·14	6·61	7·63	0·095	

*SP, spudcan; FL, flat; a, b, c represent the three sections of the drum centrifuge, respectively.
†Based on average moisture content.

specific relative density. For the non-visualising experiments performed in the drum channel, 38 mm dia. tube samples were extracted, allowing the relative density to be measured volumetrically. There is the potential that this manual sampling process caused some minor sample disturbance; however, the choice was made not to use alternative methods such as cone penetration test (CPT) correlations as the sand layer heights in these models were deemed too small to generate reliable measurements using a miniature CPT (Lunne *et al.*, 1997). The average relative densities of the sand layers were 74% in the visualising experiments and 51% in the non-visualising experiments. The constant volume friction angle (φ_{cv}) of the superfine sand was taken as 31° (after Lee *et al.*, 2013a).

Following the foundation penetration tests, epoxy ball penetrometer tests (Lee *et al.*, 2012) were conducted in the underlying clay layer after carefully removing the top clay and sand layers to minimise disturbance due to possible down-drag of sand and clay beneath the penetrometer. An intermediate roughness ball factor of $N_{ball} = 13·5$ was used to measure the in-situ undrained shear strength profile of the clay. These measurements were adjusted to account for the overconsolidation ratio (OCR) (due to removal of the sand and clay layers, which was done to preclude entrapment of material beneath the penetrometer) using the following equation after Ladd *et al.* (1977)

$$\frac{s_u}{\sigma'_{vo}} = a OCR^b \tag{1}$$

where s_u is the undrained shear strength of clay (kPa); σ'_{vo} is the present effective vertical stress (kPa); and a and b are fitting parameters that are back-fitted. From these measurements the in-situ undrained shear strength at the mudline (s_{um}), the top (clay–sand) and bottom (sand–clay) layer intercepts (s_{uti} and s_{ubi}) and the gradients of strength with depth (ρ_{ct} and ρ_{cb}) were inferred. The effective unit weights of the clay layers (γ'_{ct} and γ'_{cb}) were measured by oven drying 20 mm dia. samples extracted from each of the layers.

LOAD–PENETRATION RESPONSES DURING PUNCH-THROUGH
Visualising experiments: clay interbedded with dense sand ($I_D = 74\%$)

Figure 3 shows the 12 load–penetration curves measured during the visualising drum centrifuge experiments. The responses are grouped in Figs 3(a) and 3(c) and Figs 3(b) and 3(d) to isolate the effect of H_{ct} and H_s for the spudcan and flat foundations, respectively. In all the analyses the load reference plane is taken at the maximum base area ($A = \pi D^2/4$) of the spudcan and the nominal bearing resistance q_{nom} is defined as the net vertical load ($F_{net} = F_{total} - F_{buoyancy} - F_{friction}$; where $F_{buoyancy}$ and $F_{friction}$ were derived by the aforementioned calibration process) divided by the maximum spudcan area ($q_{nom} = F_{net}/A$). Many of the load–penetration responses show a region of reducing penetration resistance indicative of a punch-through response. For the majority of the curves the q_{nom} values are within the range (192–960 kPa) typical for jack-up operations (Young *et al.*, 1984).

For spudcans, the bearing pressure does not increase significantly until the underside of the spudcan is fully in contact with the mudline (full embedment), whereas for flat foundations the rise in resistance is immediate. The resistance increases linearly with depth because the undrained shear strength of the top clay layer increases approximately linearly with depth and the bearing factor reaches a constant value at a very shallow embedment in soft clay. Eventually the influence of the interbedded sand layer causes the resistance to rise more rapidly as the sand layer is mobilised. This is referred to as the transitional depth, d_t, because the mechanism is transitioning from a classical spudcan bearing capacity mechanism (soil flowing laterally and upwards around the spudcan) to a punch-through peak resistance type mechanism (with a block of soil beneath the spudcan being punched downwards). When this punch-through mechanism is mobilised, the peak resistance q_{peak} occurs. As the foundation punches through the sand layer into the underlying clay, the resistance initially reduces before rising once more when the spudcan is fully penetrated into the underlying clay. In this region the resistance rises because the undrained shear strength of the underlying clay layer increases with depth. The severity of the reduction in penetration resistance post-q_{peak} and the depth over which $q_{nom} < q_{peak}$ determine the severity of a punch-through type failure.

Figures 4(a) and 4(b) illustrate that q_{peak} increases with both H_{ct}/D and H_s/D. For a spudcan and intermediate normalised sand height ($H_s/D = 0·67$), increasing H_{ct}/D over the range from 0 (i.e. sand–clay) to 0·91, q_{peak} rises by $\sim 63\%$ (see Fig. 4(a)). For H_{ct}/D of $\sim 0·65$, increasing H_s/D over the range of 0·33–1 increases q_{peak} by $\sim 250\%$ (see Fig. 4(b)). Thus, H_s/D has a more significant impact on q_{peak} than H_{ct}/D for this particular series of experiments. Similar trends are evident with respect to d_{punch}, as illustrated in Figs 4(c) and 4(d): H_s/D has a dominant effect on the magnitude of d_{punch} compared to H_{ct}/D.

### Non-visualising experiments: clay interbedded with medium dense sand ($I_D = 51\%$)

Figure 5 shows the 15 load–penetration curves measured during the non-visualising drum centrifuge tests (12 spudcan and three flat foundations) performed in three different sections of the drum centrifuge channel to yield a range of normalised geometries. The general characteristics of response in clay–sand–clay are the same as described in the previous section for the visualising experiments: H_s/D dominates H_{ct}/D with respect to the magnitude of q_{peak} and d_{punch}. However, owing to the lower relative density ($I_D = 51\%$) of the sand layer the q_{peak} values are generally smaller than those of $I_D = 74\%$ in Fig. 3. Aside from this difference, one other key observation can be made from this set of data: smaller D typically leads to greater q_{peak} and more severe punch-through, whereas larger D tends to result in a plunging type failure (Hu *et al.*, 2014a) where $q_{nom} \approx q_{peak}$ for several metres. The same trend was found by Lee *et al.* (2013a) for similar sand–clay experiments.

Figure 6 isolates the effect of H_{ct} for D of 16, 8 and 6 m for tests conducted in sections b and c of the drum centrifuge channel where H_s was 4 m. By increasing H_{ct} by 2·32 m (in prototype terms), q_{peak} increased by 7, 10 and 19% for $D = 16$, 8 and 6 m, respectively. Hence, the effect of H_{ct} on q_{peak} is more significant for smaller D (i.e. greater H_{ct}/D).

Figure 7 isolates the effect of H_s for D of 16, 12 and 6 m for tests conducted in sections a and b of the drum centrifuge channel where H_{ct} was ~ 6 m. By increasing H_s by 2·25 m (in prototype terms), q_{peak} increased by 15, 30 and 30% for $D = 16$, 12 and 6 m, respectively. Hence, the effect of H_s on q_{peak} is also more significant for smaller D (i.e. greater H_s/D).

FAILURE MECHANISMS DURING PUNCH-THROUGH

This section presents the results of PIV analyses performed on the digital images captured during the visualising tests
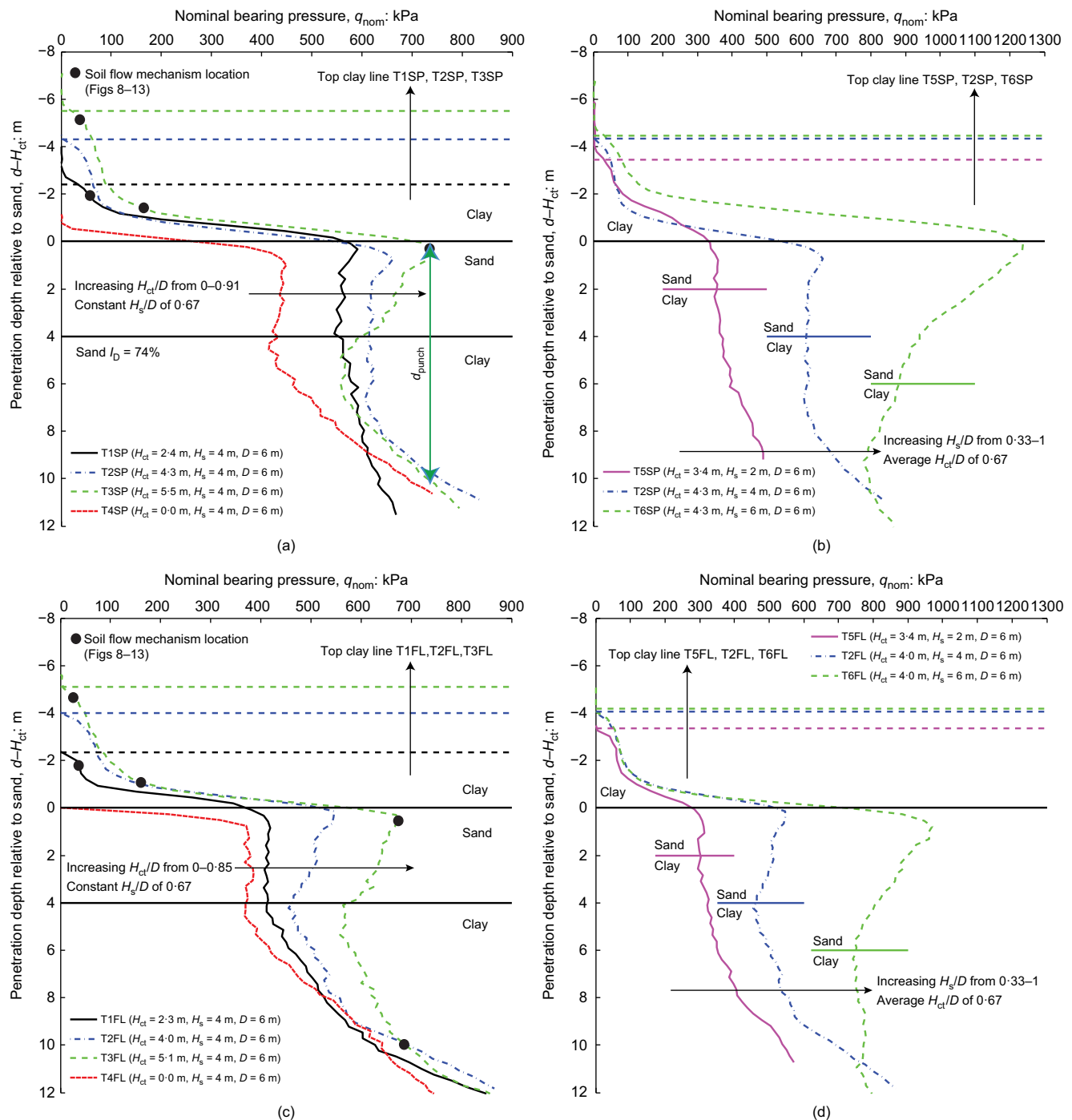
Fig. 3. Load–penetration response of (a), (b) spudcan and (c), (d) flat foundation for clay with interbedded dense sand performed in drum centrifuge strongboxes

performed in a strongbox within the drum centrifuge channel. Incremental vectorial displacements are plotted over a displacement increment of ~ 0.06 m (prototype scale) using an amplification factor of 20 for clarity. All analyses were conducted using the GeoPIV software (White *et al.*, 2003). The subset size adopted was 50×50 pixels and the spacing was 10 pixels. The vertical and horizontal displacement contours are normalised by the foundation displacement and plotted over the range of 0·1–1, at increments of 0·1. A normalised incremental displacement of unity indicates that the surrounding material moves at the same velocity as the foundation. In all cases, the top of the sand layer was taken as the vertical datum and the foundation size D was 6 m for consistency with Fig. 3 where the depths and penetration resistances of each analysis are indicated.

Effect of H_{ct} *on failure mechanisms in the top clay layer*

The failure mechanisms for a spudcan (test T1SP) and flat foundation (test T1FL) in a thin top clay layer are shown at a penetration of ~ 0.5 m from the mudline in Fig. 8. When the top layer of clay is thin – as shown in Fig. 8 – the soil immediately squeezes radially because the comparatively strong layer of sand beneath it confines the failure mechanism to the upper clay layer. This is similar to the squeezing behaviour explored by Meyerhof & Chaplin (1953) except that some vertical component of soil movement is also noted. However, the occurrence of this effect is dependent upon the top clay layer height. When the top clay layer is thick – as shown in Fig. 9 – the mechanisms resemble those typical of shallow foundations; in particular, the cavity expansion model of McMahon *et al.* (2013).
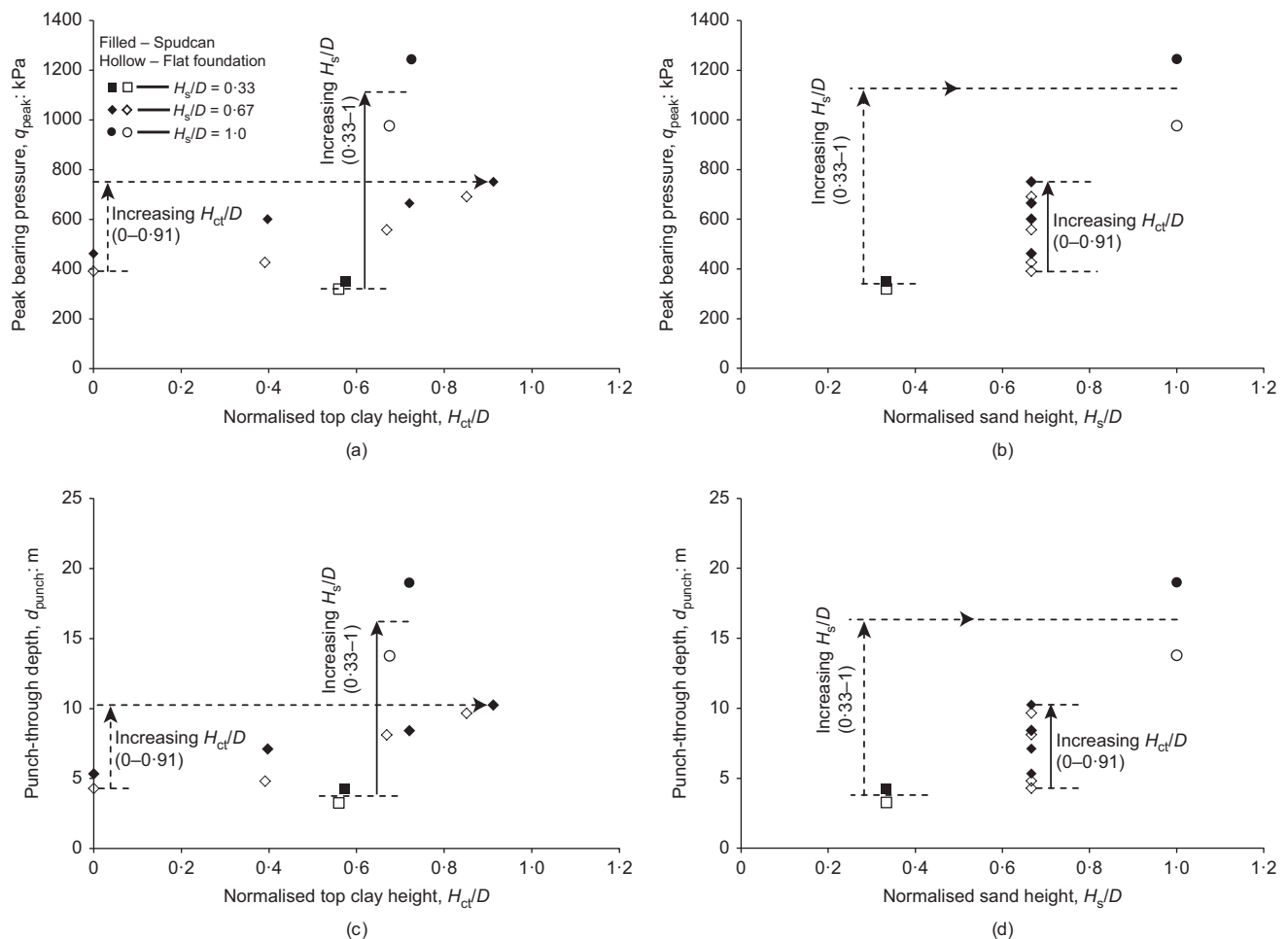
Fig. 4. Effect of H_s/D and H_{ct}/D on q_{peak} and d_{punch}: (a) q_{peak} plotted against normalised clay height H_{ct}/D; (b) q_{peak} plotted against normalised sand height H_s/D; (c) d_{punch} plotted against normalised clay height H_{ct}/D; (d) d_{punch} plotted against normalised sand height H_s/D

The expected squeezing mechanism in clay as identified in Fig. 8 is not evident in the thick top clay layer when the foundations approach the sand layer. Fig. 10 shows the failure mechanisms when the foundations are in close proximity to the sand layer and it is clear that the radial squeezing is minimal. This observation is similar to that derived by way of similar PIV tests performed with a larger foundation ($D = 12$ m) penetrating soft over stiff clay (Hossain *et al.*, 2011). These findings contradict the current industry guidelines (SNAME, 2008; ISO, 2012) where radial soil squeezing is assumed for soft over stiff stratigraphies, irrespective of the soft layer height. Possible reasons for the deviation from the squeezing theory include: (*a*) that the theory of Meyerhof & Chaplin (1953) is based on soft over rigid stratum (i.e. Young's modulus, $E = \infty$), whereas here although the interbedded sand is comparatively strong, the stiffness is finite; and (*b*) as a consequence of (*a*) the sand layer deforms vertically, thus discouraging radial squeezing.

Peak failure mechanisms

The failure mechanisms at q_{peak} are shown in Fig. 11. An inverted truncated cone of clay and sand is shown to be pushed into the bottom clay layer. Both the clay and sand appear to shear along the periphery of the inverted truncated cone of soil, as indicated by the displacement magnitudes in the vector plot (Figs 11(a) and 11(d)) and the closeness of the vertical displacement contours (Figs 11(b) and 11(e)). In the underlying clay layer, the displacements appear broadly

similar to those that occurred in the thick clay layer (Fig. 9), indicating that the bearing capacity generated by the clay layer could potentially be approximated using simple shallow foundation bearing capacity expressions following Lee *et al.* (2013b). Some load spreading is evident because the width mobilised at the surface of the bottom clay layer is larger than the foundation diameter, although the inclination of this load spreading is of the order of a few degrees and significantly less than the ~11–18° recommended in the projected area method in the current industry guidelines (SNAME, 2008; ISO, 2012). A partial back flow of clay above the foundation is also apparent, which leads to a reduction in capacity as it causes an increase in the vertical loading. The failure mechanism at q_{peak} is not significantly different for the flat foundation compared to the spudcan.

The digital images captured during these experiments were further interrogated to derive general geometries of the soil failure mechanisms for foundation peak resistances (Fig. 12(a)). The images showed that a thin band of clay (of height H_c) was entrapped beneath the foundation and sheared during mobilisation of the peak resistance. Measurement of the entrapped clay layer geometry using close-range photogrammetry (see Fig. 12(b)) yielded the following linear relationship between the entrapped clay layer height H_c and the in-situ top clay layer height H_{ct}

$$H_c = 0.07 H_{ct} \qquad (2)$$

This means, on average, 7% of the top clay layer height was entrapped beneath the foundation (for both flat and spudcan
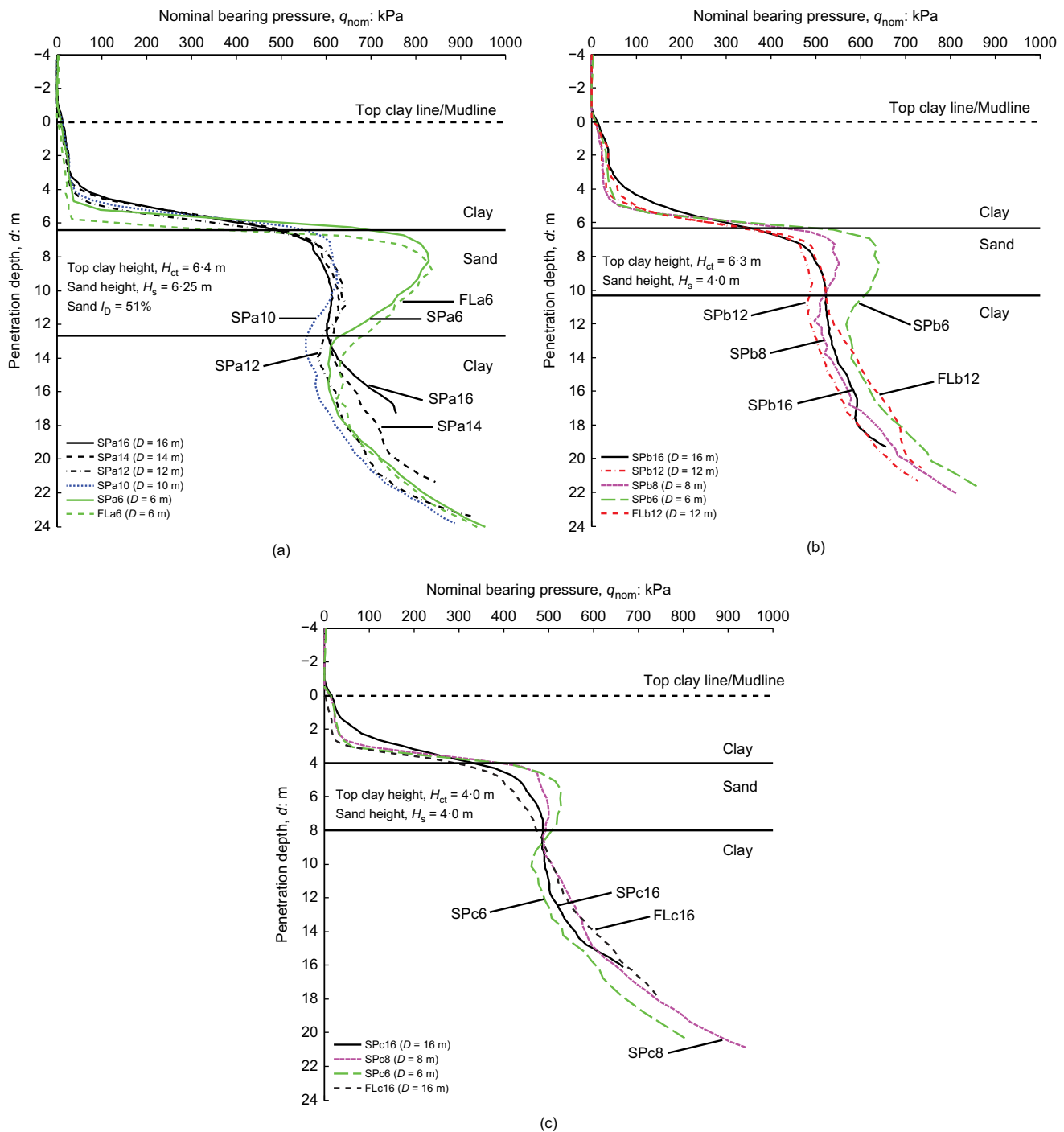
Fig. 5. Load–penetration responses for spudcan and flat foundations in clay interbedded with medium dense sand performed in the drum centrifuge channel: (a) section a; (b) section b; (c) section c

foundations tested here). For the limiting case where H_{ct} is zero (i.e. sand–clay), H_c is zero.

Similarly, the effective sand height (H_{eff}) during shearing was measured from the images and is compared with the previous reported measurements in sand–clay experiments in Fig. 12(c). The following relation, identified originally by Teh *et al.* (2008), appears to be equally valid for clay–sand–clay stratigraphies

$$H_{eff} = 0.88H_s \qquad (3)$$

The depth of mobilisation of peak resistance, d_{peak}, can be estimated from the schematic diagram in Fig. 12(a) as follows

$$d_{peak} = H_{ct} + 0.12H_s - H_c \qquad (4)$$

As the entrapped plug thickness (H_c plus H_s) increases, d_{peak} reduces (i.e. the peak resistance is mobilised earlier during the penetration). By combining equations (2) and (4), d_{peak} can be expressed as a function of the in-situ layer heights as follows

$$d_{peak} = 0.93H_{ct} + 0.12H_s \qquad (5)$$

The measured and predicted d_{peak} values from equation (5) show reasonable agreement with the majority of the predictions falling within 25% bounds (see Fig. 12(d)). The good agreements between the predictions and measurements in Figs 12(c) and 12(d) provide the potential scope for the two-layer (sand–clay) model of Hu *et al.* (2014a, 2014b) to be extended to three-layer (clay–sand–clay) geometries.
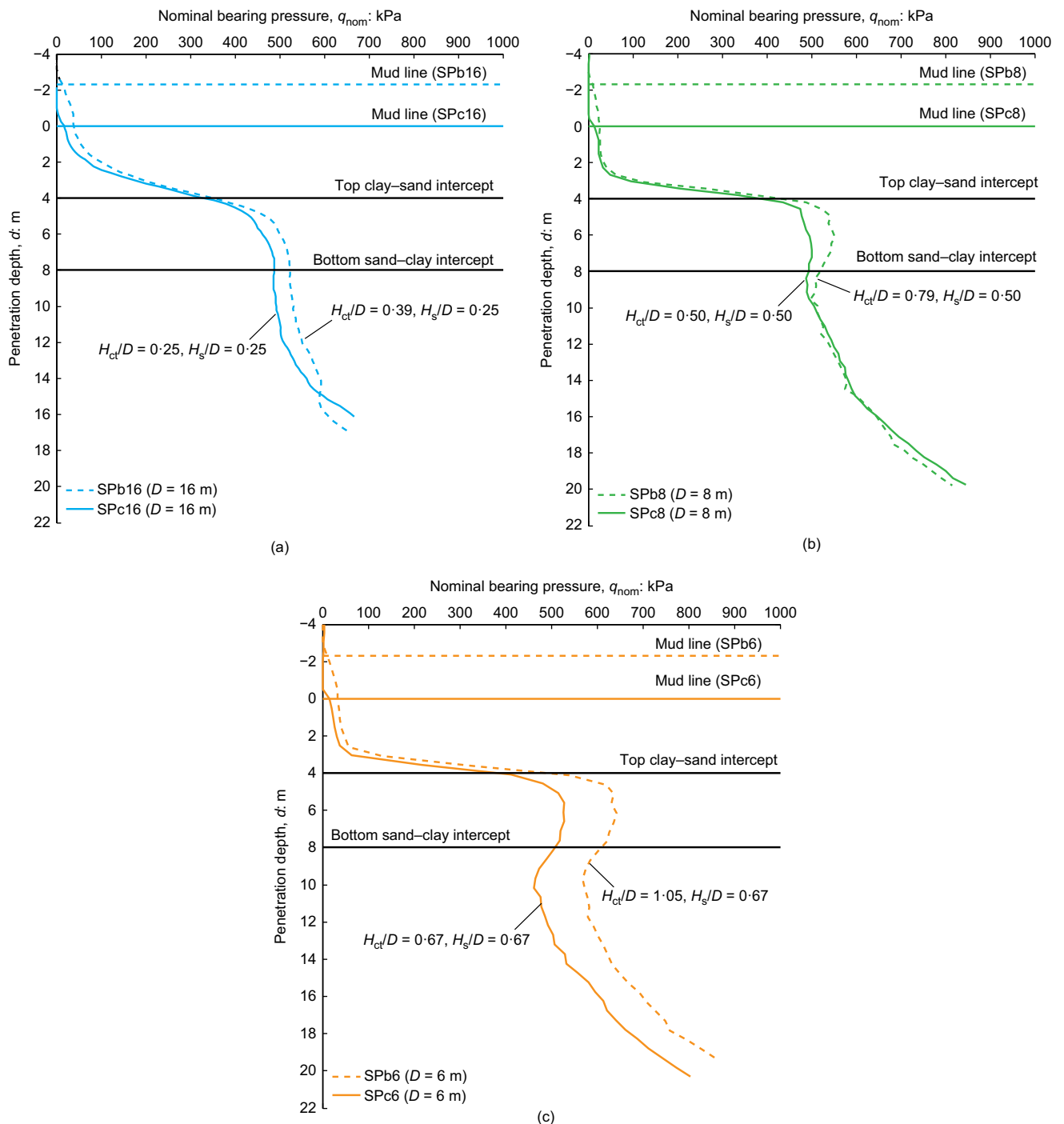
Fig. 6. Effect of H_{ct}/D on the overall penetration resistance profile in medium dense sand (section b: $H_{ct} = 6 \cdot 32$ m, $H_s = 4$ m and section c: $H_{ct} = 4$ m, $H_s = 4$ m)

Bearing capacity mechanism in the underlying clay

Figure 13 shows that a plug of soil is entrapped beneath the foundation during penetration into the underlying clay layer. The plug is composed of a thin layer of clay and thicker layer of sand, the thicknesses of which can be predicted using equations (2) and (3). In the spudcan foundation tests, the view from the transparent window showed that the size of the entrapped plug was reducing with further penetration into the underlying clay layer. Initially this was thought to be due to the conical underside of the foundation encouraging the soil within the plug to flow around the footing, since the reduction in the sand plug size was not observed in the flat foundation tests. However, comparing the bearing capacity factor N_c (= q_{nom}/s_u) after penetration of $0 \cdot 5D$ and $1D$ into

the bottom clay layer for spudcan and flat foundations for all layer geometries, the bearing capacity factors were found to be almost identical irrespective of whether the soil plug size appeared to diminish in the images. This makes it unlikely that the entrapped plug was reducing in volume during penetration. Instead, it is possible that the conical underside of the spudcan encourages the sand in the plug to flow away from the transparent window of the strongbox. This is further confirmed by the post-dissected full spudcan sample data in clay–sand–clay presented in Hossain (2014), where a sand plug depth of $0 \cdot 85$–$0 \cdot 9H_s$ was consistently measured.

Figure 13 shows the deeply embedded bearing capacity mechanism for one of the flat foundation tests (T3FL). The majority of the plug is moving vertically downward
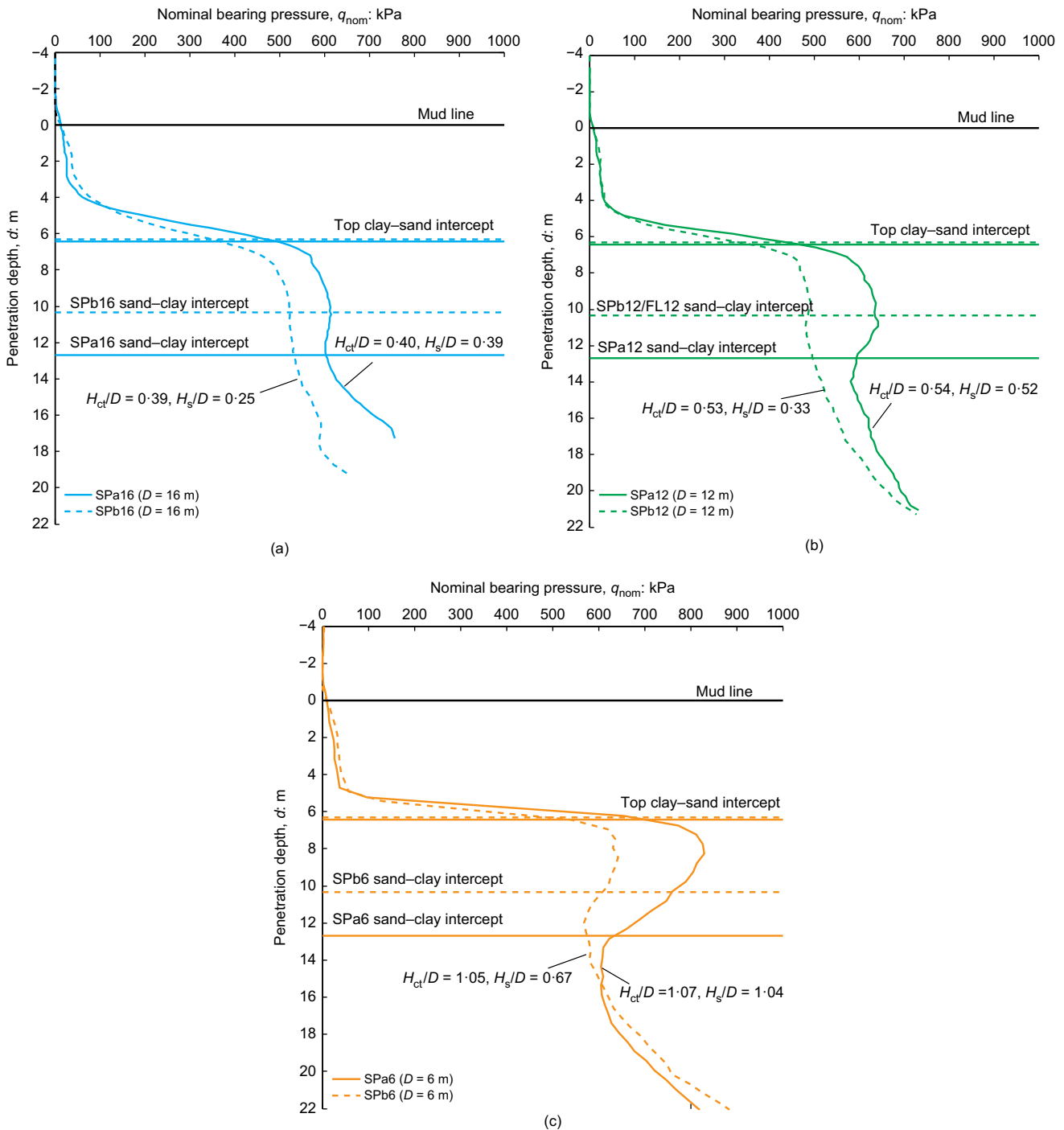
Fig. 7. Effect of H_s/D on the overall penetration resistance profile in medium dense sand (section a: $H_{ct} = 6.42$ m, $H_s = 6.25$ m and section b: $H_{ct} = 6.32$ m, $H_s = 4$ m)

with the foundation and a small triangular wedge is also formed beneath the plug. The closeness of the vertical contours indicates that the clay surrounding the plug periphery is shearing. Overall the mechanism looks very similar to that identified for sand–clay stratigraphies by Teh *et al.* (2008), except that a thin layer of clay is entrapped immediately beneath the foundation. Values for N_c were back-calculated from the q_{nom} measurements as follows

$$N_c = \frac{(q_{nom} - \gamma'_{cb} H_{fdn})}{s_u} \qquad (6)$$

where s_u is the undrained shear strength at the base of the foundation (i.e. at the load reference plane) and H_{fdn} is

defined using the schematic diagram in Fig. 12(a) as

$$H_{fdn} = 0.88 H_s + 0.07 H_{ct} + t \qquad (7)$$

where t is the foundation thickness. The N_c values varied in the range of $\sim$13–24 with greater entrapped plug volumes leading to higher N_c values. These values are much higher than those measured and simulated using large-deformation finite-element analyses reported by Hossain & Randolph (2009) for spudcan penetration in a single clay layer, where N_c was shown to be $\sim$12–13. Such large N_c values are a direct result of the large soil plug entrapment under the foundation where the height of the composite foundation can be estimated using equation (7) above. The increased height of
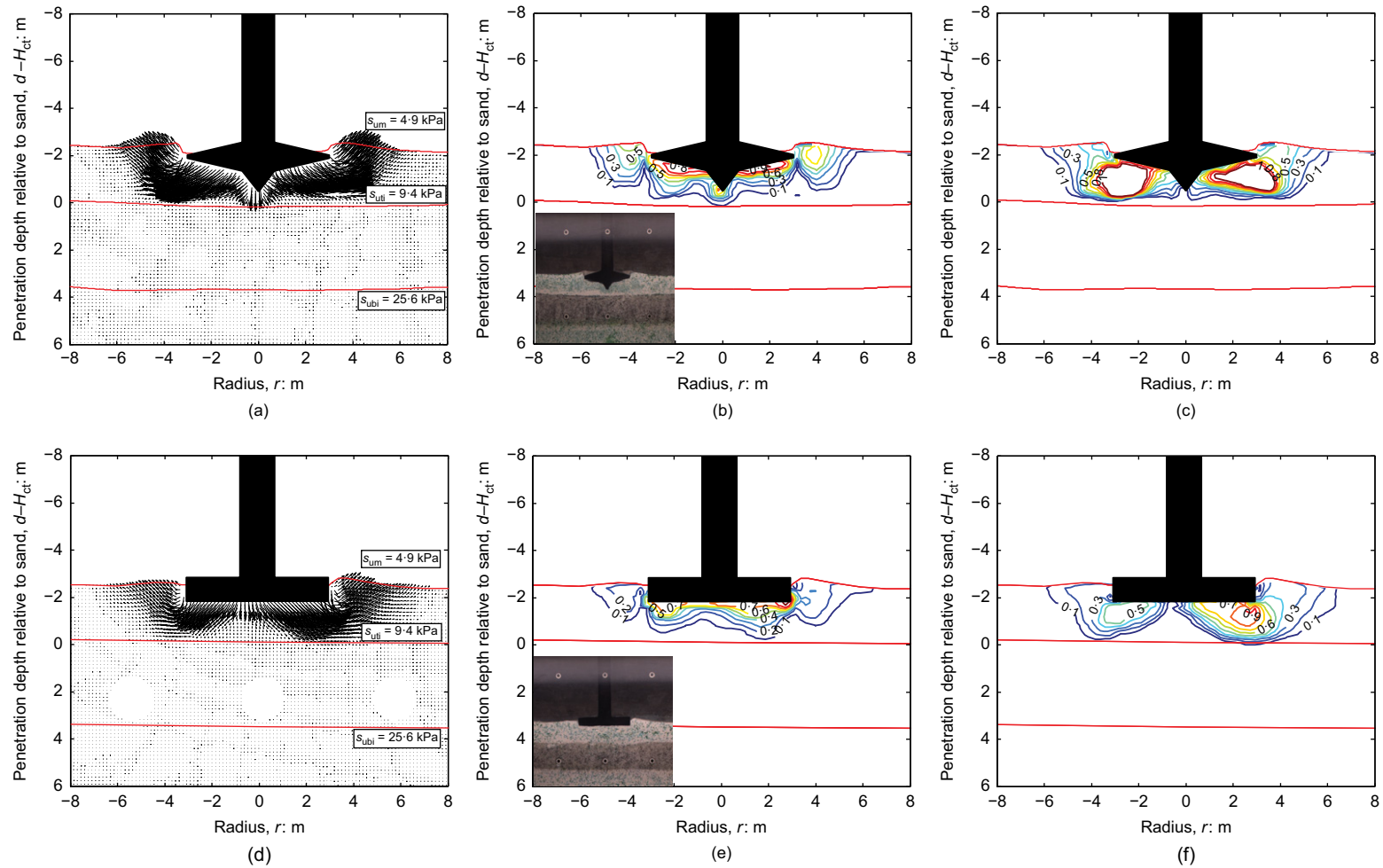
Fig. 8. Soil displacements for a thin top clay layer at a penetration depth of ∼0·5 m from the mudline for spudcan and flat foundations, respectively (T3SP, T3FL): (a), (d) vectorial displacements; (b), (e) normalised vertical displacement contours; (c), (f) normalised horizontal displacement contours
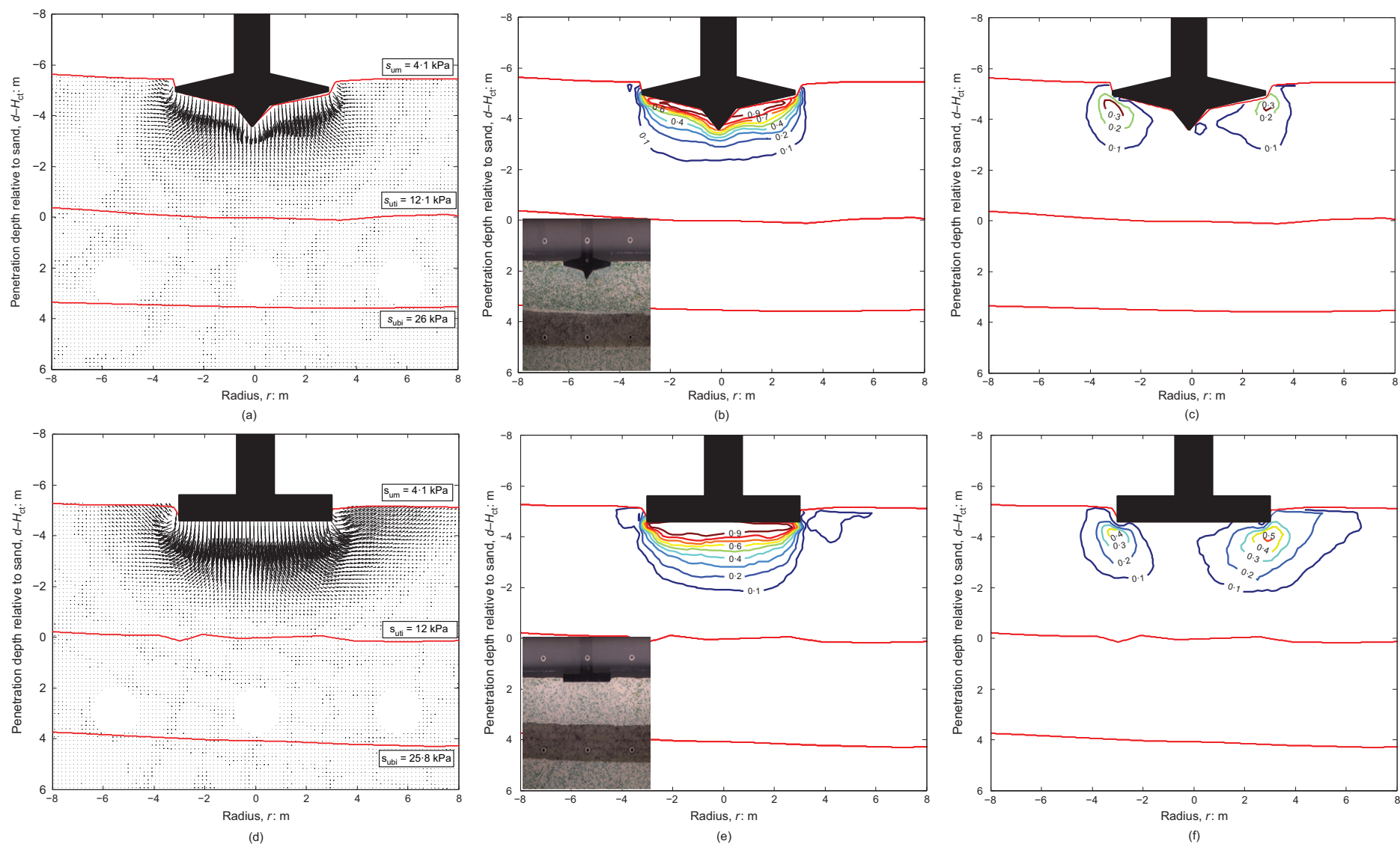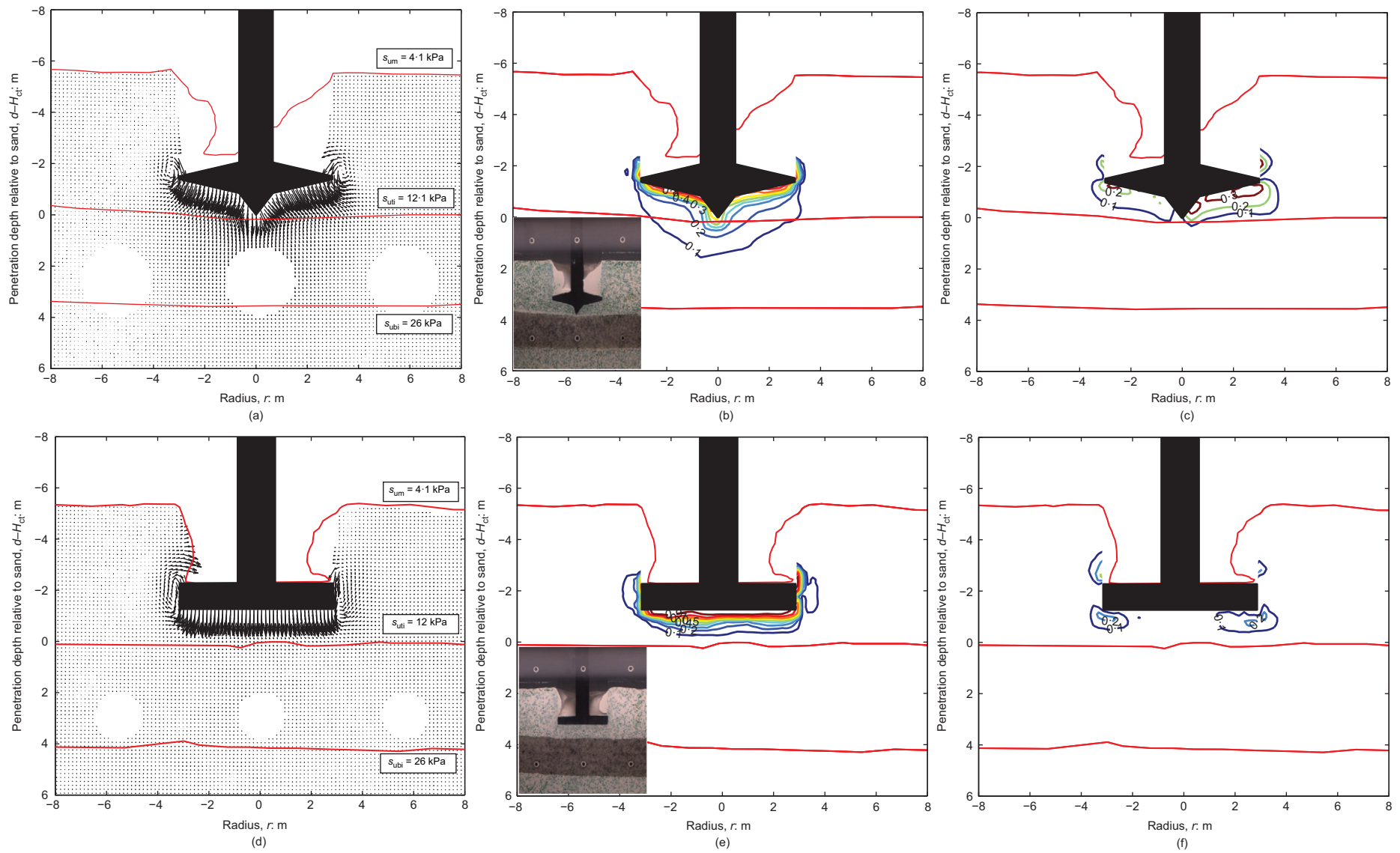
Fig. 9. Soil displacements for a thick top clay layer at a penetration depth of ~0·5 m from the mudline for spudcan and flat foundations respectively (T1SP, T1FL): (a), (d) vectorial displacements; (b), (e) normalised vertical displacement contours; (c), (f) normalised horizontal displacement contours

Fig. 10. Soil displacements when in close proximity to the sand layer for spudcan and flat foundations respectively (T2SP, T2FL): (a), (d) vectorial displacements; (b), (e) normalised vertical displacement contours; (c), (f) normalised horizontal displacement contours
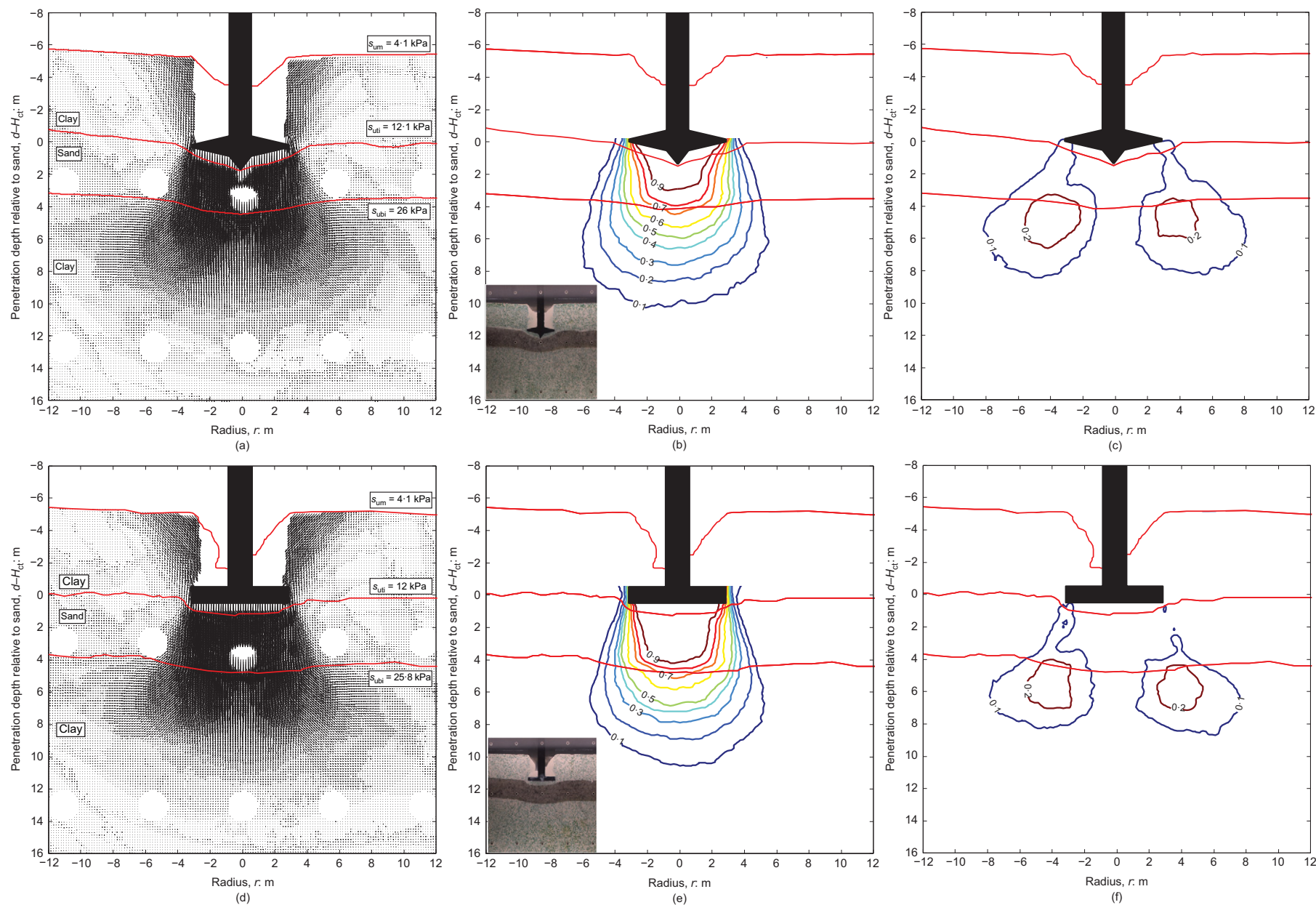
Fig. 11. Soil displacements at peak resistance for spudcan and flat foundations respectively (T3SP, T3FL): (a), (d) vectorial displacements; (b), (e) normalised vertical displacement contours; (c), (f) normalised horizontal displacement contours
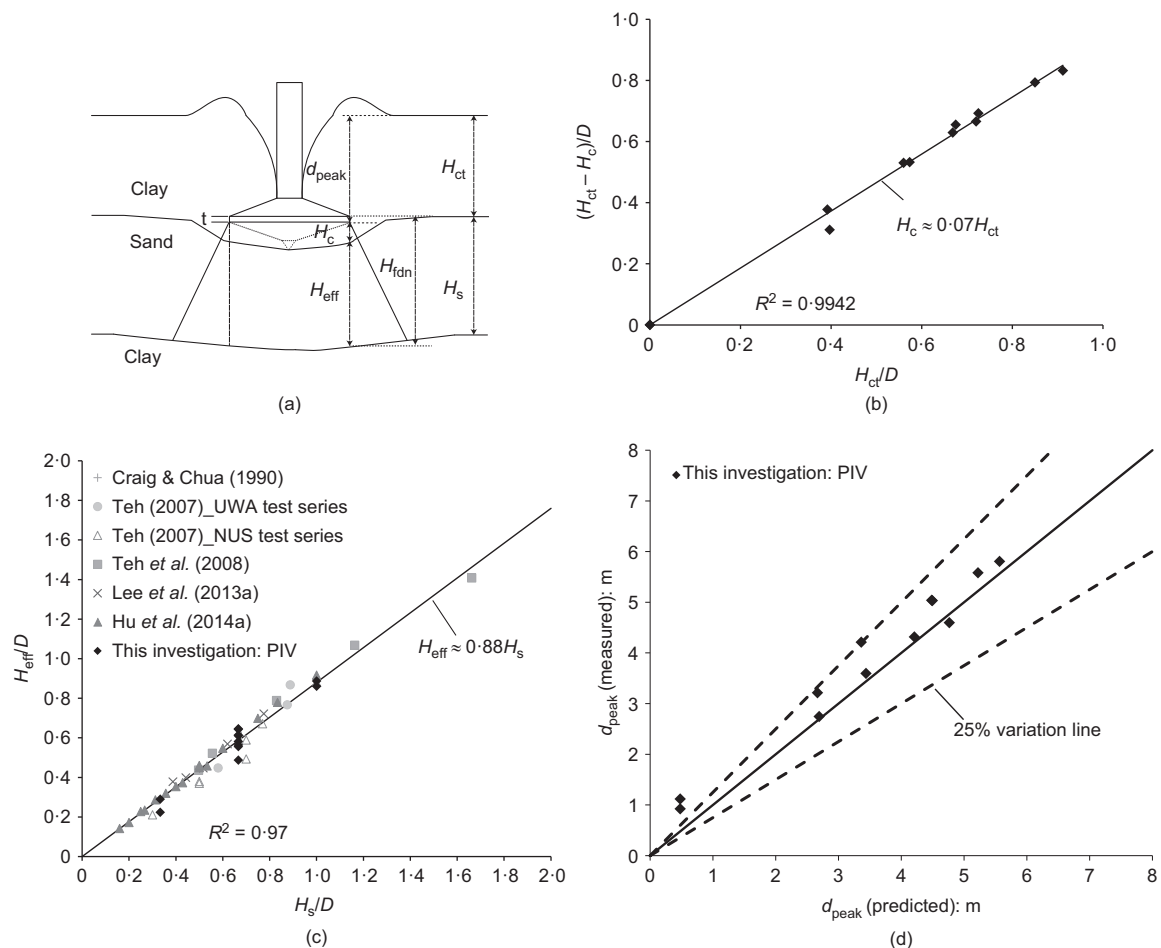
Fig. 12. (a) Geometric definitions of effective sand height (H_{eff}) and height of entrapped clay (H_c); the observed relationship between (b) H_c and in-situ clay height H_{ct}; (c) H_{eff} and H_s; and (d) the measured and predicted peak resistance depths (d_{peak})
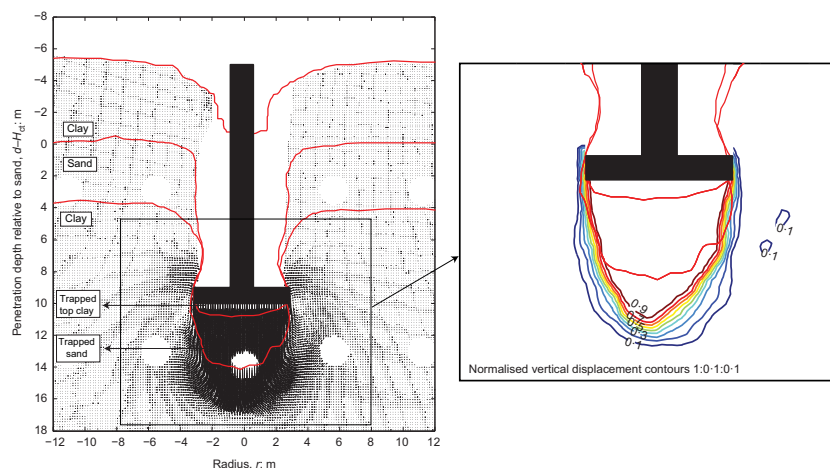

Fig. 13. Clay–sand plug entrapment during penetration into the underlying clay layer for a flat foundation test (T3FL)

the composite foundation provides additional shear resistance around the entrapped plug periphery and mobilises deeper soil with a higher strength than the s_u value used in the definition of N_c at the foundation base level (Craig & Chua, 1990) resulting in higher N_c values than for penetration into a single layer of clay. For sand over clay soil, large N_c values over a similar range as observed here were obtained by Lee *et al.* (2013a) through centrifuge testing and by Hu *et al.* (2014a) through large-deformation finite-element analyses. For a comprehensive assessment of the performance of the equations derived here (equations (5)–(7)) see the companion paper of Ullah *et al.* (2016a).

PERFORMANCE OF CURRENT INDUSTRY APPROACHES FOR PREDICTING PUNCH-THROUGH

The peak bearing capacity (q_{peak}) determines the amount of preload that can be safely applied to the foundation without inducing punch-through failure. Accurate q_{peak}

prediction is therefore extremely important. In addition, prior to installing a jack-up foundation, a complete punch-through risk assessment typically involves determining the potential depth of the punch-through event, d_{punch}.

The existing industry guidelines (SNAME, 2008; ISO, 2012) recommend the projected area (PA) (also known as load-spread) and punching shear (PS) methods. In the PA approach, upper and lower bound projection angles (α_p) corresponding to $18\cdot43°$ (1h:3v where 'h' is horizontal, 'v' is vertical) and $11\cdot31°$ (1h:5v) are recommended in both guidelines. In the PS approach, the SNAME (2008) and ISO (2012) guidelines differ in their recommendations of choosing a suitable punching shear coefficient, K_s. SNAME (2008) recommends choosing a lower bound K_s where the sand frictional properties are ignored and replaced with clay strength properties as follows

$$K_s \tan \phi' = \frac{N s_{ubi}}{\gamma_s' D} \quad (8)$$

where φ' is the peak operative friction angle, γ_s' is the sand effective unit weight and s_{ubi} is the bottom sand–clay intercept strength. A lower bound value of $N = 3$ is recommended. Alternatively, ISO (2012) provides a single design chart for estimation of K_s after Hanna & Meyerhof (1980) for friction angles (φ') of 25–40° at 5° intervals. Interpolation or extrapolation is required for intermediate

values. The typical range for K_s is between $\sim 0\cdot5$ and 12. There is no clear recommendation for choosing the operative friction angle when estimating K_s. A constant-volume friction angle ($\varphi' = \varphi_{cv}$) was assumed in these predictions.

As noted by Hu *et al.* (2015) there is some ambiguity in the ISO (2012) guidelines regarding the position of the surcharge in the calculations. To comprehensively explore the performance of the existing industry guidelines, calculations were performed by both considering and ignoring the effective weight of the sand frustum (W_{SF}) when calculating the surcharge term. In the PA method, when neglecting the effect of the weight of the sand plug (hollow markers) the expression used was

$$q_{peak} = \left[(s_c N_c s_{ubi} + q_o) \left(1 + 2 \frac{H_s}{D} \tan \alpha_p \right)^2 \right] \quad (9)$$

whereas when accounting for the weight of the sand plug (filled markers) the expression used was

$$q_{peak} = \left[(s_c N_c s_{ubi} + q_o) \left(1 + 2 \frac{H_s}{D} \tan \alpha_p \right)^2 \right] - \left[\left(1 + 2 \frac{H_s}{D} \tan \alpha_p \right)^2 \gamma_s' H_s \right] \quad (10)$$
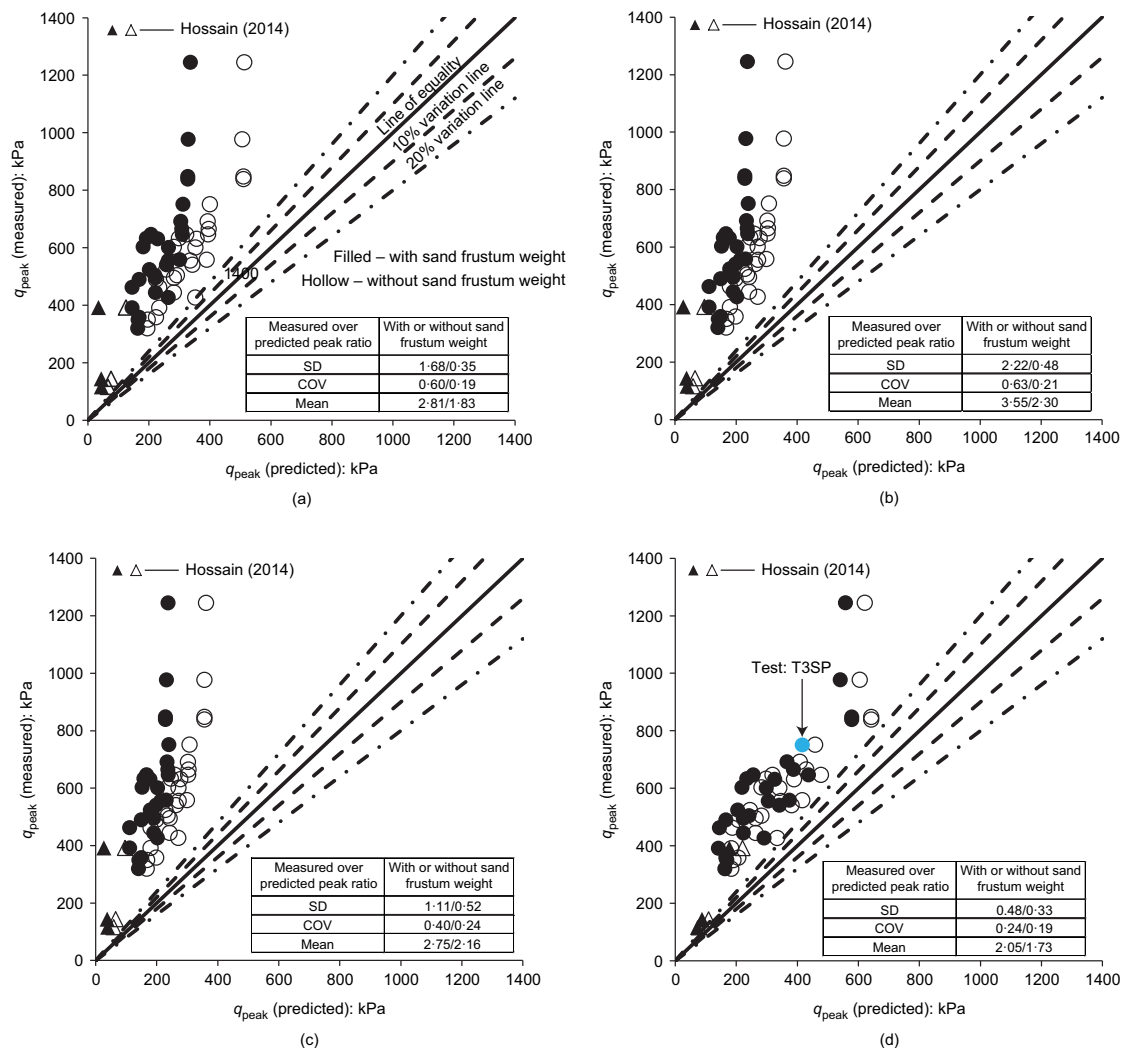
Fig. 14. Performance of current industrial guideline approaches in predicting q_{peak}: (a) projected area or load-spread method with spread ratio of 1h:3v; (b) projected area or load-spread method with spread ratio of 1h:5v; (c) SNAME (2008) punching shear approach; (d) ISO (2012) punching shear approach

Similarly, in the PS method, when neglecting the effect of the weight of the sand plug (hollow markers) the expression used was

$$q_{\text{peak}} = (s_c N_c s_{\text{ubi}} + q_o)$$
$$+ \left[2 \frac{H_s}{D} (\gamma'_s H_s + 2q_o) s_s K_s \tan \phi' \right] \quad (11)$$

whereas when accounting for the weight of the sand plug (filled markers) the expression used was

$$q_{\text{peak}} = (s_c N_c s_{\text{ubi}} + q_o)$$
$$+ \left[2 \frac{H_s}{D} (\gamma'_s H_s + 2q_o) s_s K_s \tan \phi' \right] - \gamma'_s H_s \quad (12)$$

Here, s_s represents the shape factor and is assumed as 1. Both PA and PS methods recommended in the guidelines are for two-layer stiff over soft soil conditions. The effect of the top soft clay (H_{ct}) was accounted for in the predictions in this paper by assuming that the top clay layer acts as a further surcharge

$$q_o = H_{\text{ct}} \gamma'_{\text{ct}} \quad (13)$$

where γ'_{ct} is the effective unit weight of the top clay.

The performance of these two methods and both interpretations (accounting for and neglecting the self-weight of the sand plug) are shown in Fig. 14. In addition to the experimental data reported in this paper, three tests on clay–sand–clay ($I_D = 89\%$) reported by Hossain (2014) have been added. Both PA and PS approaches underestimate q_{peak}. In all cases neglecting the effective sand frustum weight provides a minor improvement in the q_{peak} estimation, leading to small improvements in the statistical parameters the ratio of measured to calculated q_{peak} (mean, standard deviation (SD) and coefficient of variation (COV)). The predictions can only be forced to converge with the measurements by either: (a) adopting very high values of α_p for the PA method, thus implying extremely high load-spread angles (i.e. higher than the ~11–18° range recommended in industry guidelines) that would contradict the PIV observations in Fig. 11; or (b) adopting very high values for the punching shear coefficient K_s. There is no rational basis for either modification.

The conservative predictions generated by the PA and PS approaches are similar to those found for the two layers of the sand–clay case (Hu et al., 2015). For the two-layer sand–clay case, such conservatism principally occurs because neither method accounts for the stress-level-dependent response of the sand shearing at mobilisation of q_{peak} (as seen here in
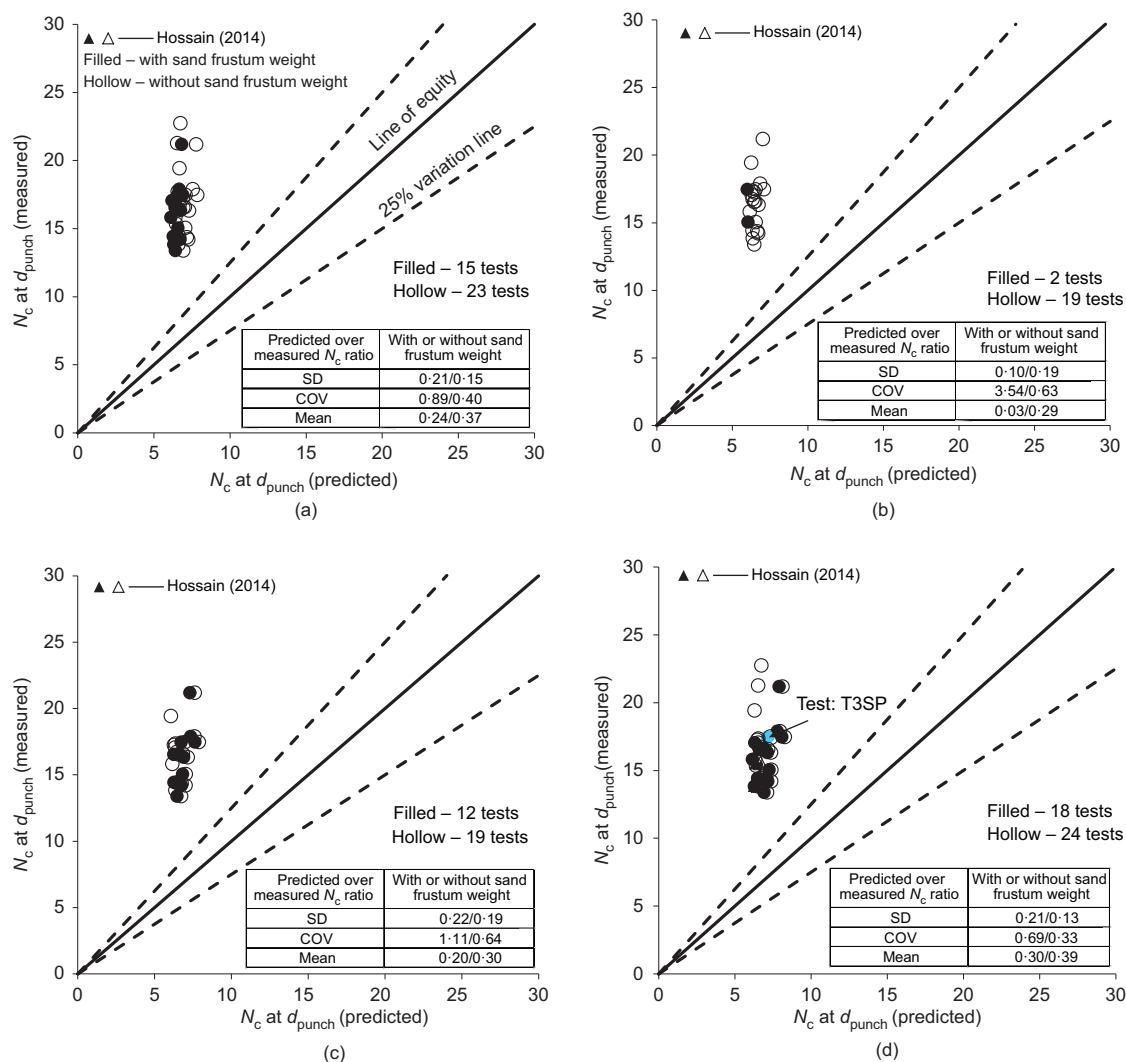

Fig. 15. Performance of current industrial guideline approaches in predicting N_c at $q_{\text{clay}} = q_{\text{peak}}$: (a) projected area or load-spread method with spread ratio of 1h:3v; (b) projected area or load-spread method with spread ratio of 1h:5v; (c) SNAME (2008) punching shear approach; (d) ISO (2012) punching shear approach

Fig. 12 for the three-layer clay–sand–clay case). This indicates that development of a stress-level-dependent approach for predicting q_{peak} – like that described by Hu *et al.* (2014a) for the sand–clay case – would likely lead to improvements in the predictions for the clay–sand–clay cases presented here.

Estimation of d_{punch} requires accurate estimation of both q_{peak} and the bearing capacity factor (N_c) for the bottom clay layer at a depth where $q_{nom} = q_{peak}$ (see Fig. 3(a)). For the SNAME (2008) and ISO (2012) methods, N_c is recommended to be calculated after Houlsby & Martin (2003). The equivalent cone angle β was 180° and 154° for flat and spudcan foundations, respectively, with the surface roughness α taken as 0·2 following Hossain *et al.* (2005), as the foundations had a smooth finish.

Figure 15 shows the measured N_c plotted against the predicted N_c at d_{punch} indicating that the N_c values predicted using Houlsby & Martin (2003) are extremely conservative because the presence of the entrapped sand plug observed in Fig. 13 is unaccounted for.

The impact that this consistent conservatism has on the d_{punch} predictions in Fig. 16 is fortuitous: under-predictions for q_{peak} and N_c result in generally acceptable predictions of d_{punch} for all methods. One example of the beneficial effect of these compensating errors is highlighted in Figs 14–16

(test T3SP; see also Fig. 3) for the ISO (2012) PS approach (blue marker, shown with an arrow): although q_{peak} and N_c are underestimated by $\sim 40\%$ (Fig. 14) and by $\sim 58\%$ (Fig. 15), respectively, d_{punch} is predicted very well due to the compensating errors and falls on the line of equality (Fig. 16). Additionally, the under-predictions of q_{peak} lead to a number of cases where punch-through was not predicted, even though punch-through of several metres occurred (at prototype scale) and was observed in the experiments. Alternative expressions for predicting q_{peak} and N_c that explicitly account for stress-level-dependent sand response and the presence of the entrapped plug are required to generate reliable assessments for the risk of punch-through for clay–sand–clay stratigraphies. To improve on the industry guidelines, the current authors have developed an extension of the analytical model of Hu *et al.* (2014a) based on the observed PIV failure mechanisms that has been reported in the companion paper (see Ullah *et al.*, 2016a).

CONCLUSIONS

Centrifuge tests modelling foundation punch-through on clay–sand–clay stratigraphies of varying geometry have been reported for both conical spudcan and flat-based foundation shapes. Two series of experiments were described (visualising
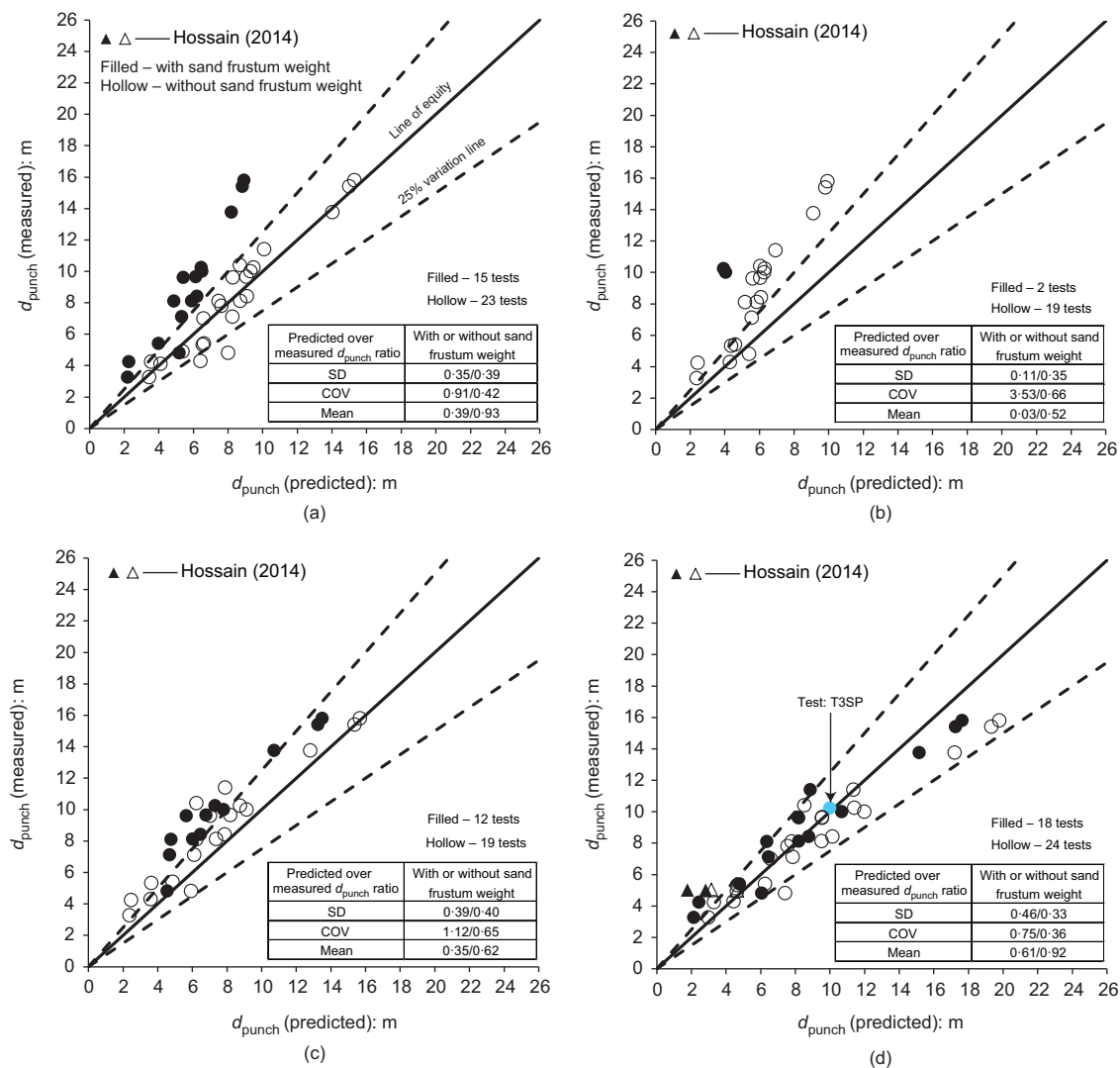

Fig. 16. Performance of current industrial guideline approaches in predicting d_{punch}: (a) projected area or load-spread method with spread ratio of 1h:3v; (b) projected area or load-spread method with spread ratio of 1h:5v; (c) SNAME (2008) punching shear approach; (d) ISO (2012) punching shear approach

strongbox and non-visualising full drum channel tests) resulting in a database of 27 load–displacement curves for clay interbedded with both medium dense and dense sand. Punch-through was observed for a wide range of stratigraphy geometries. Digital images recorded during the visualising experiments were analysed using PIV techniques to identify the soil flow mechanisms at key stages during punch-through. The peak resistance q_{peak}, bearing capacity factor N_c where $q_{nom} = q_{peak}$ and the depth of punch-through d_{punch} were predicted using current industry guidelines and compared to measurements from the experiments. This led to the following conclusions.

- q_{peak} is dependent on both the normalised top clay height (H_{ct}/D) and sand height (H_s/D). For constant H_{ct}/D, increasing H_s/D results in a significant increase in q_{peak}. For constant H_s/D, increasing H_{ct}/D also results in a moderate increase in q_{peak}.
- The failure mechanism in the top clay layer was controlled by H_{ct}/D in the experiments presented in this paper, with progressively lower H_{ct}/D values promoting more radial squeezing of soil. Owing to differences in mechanisms, the soft over stiff soil squeezing theories recommended by ISO (2012) and SNAME (2008) are not generally applicable in modelling the rapid increase in resistance above the sand layer. Alternative methods of predicting the resistance in the top clay layer are required.
- During mobilisation of q_{peak} a thin band of top clay becomes entrapped beneath the foundation and shears at the periphery of the foundation along with sand beneath. A load-spreading type mechanism occurs where the load is projected onto a larger bearing area on the bottom clay than the foundation area. Simple expressions were derived from measurements of the geometries at q_{peak} using the digital images. The heights of the entrapped clay layer (H_c), effective sand layer height (H_{eff}) and the depth of the peak resistance (d_{peak}) were all shown to depend on the intact layer heights.
- A composite soil plug comprising entrapped layers of clay and sand was shown to be pushed down into the bottom clay layer following punch-through. This generated additional shearing resistance because clay around the periphery of the entrapped plug sheared during further penetration. This results in a significant increase in bearing capacity factor N_c compared to either the Houlsby & Martin (2003) relation recommended by SNAME (2008) and ISO (2012) or those derived for a spudcan on single layer clay by Hossain & Randolph (2009).
- The current industrial guidelines provided by SNAME (2008) and ISO (2012) are overly conservative in predicting q_{peak} and N_c where $q_{nom} = q_{peak}$. The compensating errors fortuitously result in generally acceptable prediction of the punch-through depth d_{punch}. However, many cases where punch-through occurred in the experiments were predicted to not be at risk of punch-through. Alternative expressions for predicting q_{peak} and N_c – that explicitly account for stress-level-dependent sand response and the presence of the entrapped plug – are required to generate reliable assessments for the risk of punch-through for clay–sand–clay stratigraphies.
- The experiments reported provide a database for developing and verifying an extension of the stress-level-dependent punch-through models for sand–clay stratigraphies (Lee *et al.*, 2013b; Hu *et al.*, 2014a) to account for the presence of the overlying clay layer in clay–sand–clay stratigraphies.

NOTATION

A	bearing area of circular foundation
a	fitting parameter in OCR equation
b	fitting parameter in OCR equation
c_v	coefficient of consolidation
D	foundation diameter
d	foundation penetration depth
d_{peak}	depth of peak position
d_{punch}	punch-through depth
E	Young's modulus
e_{max}	maximum void ratio
e_{min}	minimum void ratio
$F_{buoyancy}$	foundation buoyancy force
$F_{friction}$	force due to window friction
F_{net}	net vertical load
F_{total}	total vertical load
g	Earth's gravitational acceleration
H_c	height of trapped clay
H_{ct}	height of top clay
H_{eff}	effective sand height
H_{fdn}	height of composite foundation
H_s	height of sand
I_D	sand relative density
K_s	coefficient of punching shear
N_c	clay bearing capacity factor
q_{nom}	nominal bearing pressure
q_o	surcharge
q_{peak}	peak bearing capacity
s_c	shape bearing capacity factor due to cohesion
s_s	shape factor in punching shear method
s_u	undrained shear strength of clay
s_{ubi}	bottom sand clay intercept strength in clay–sand–clay
s_{um}	undrained clay strength at mudline
s_{uti}	top sand clay intercept strength in clay–sand–clay
t	thickness of foundation
V	non-dimensional velocity
v	penetration velocity
W_{SF}	weight of sand frustum
α_p	projection angle in sand layer
β	equivalent conical angle
γ'_{cb}	bottom clay effective unit weight
γ'_{ct}	top clay effective unit weight
γ'_s	sand effective unit weight
ρ_{bt}	bottom clay undrained shear strength gradient
ρ_{ct}	top clay undrained shear strength gradient
σ'_{vo}	in-situ effective vertical stress
υ	foundation penetration velocity
φ_{cv}	constant volume friction angle
φ'	operative friction angle

REFERENCES

Baglioni, V. P., Chow, G. S. & Endley, S. N. (1982). Jack-up rig foundation stability in stratified soil profiles. *Proceedings of the offshore technology conference*, Houston, TX, USA, paper OTC 4409, pp. 363–384.

Bienen, B. & Cassidy, M. J. (2013). Set up and resulting punch-through risk of jack-up spudcans during installation. *J. Geotech. Geoenviron. Engng* **139**, No. 12, 2048–2059.

Bienen, B., Ragni, R., Cassidy, M. J. & Stanier, S. A. (2015). Effects of consolidation under a penetrating footing in carbonate silty clay. *J. Geotech. Geoenviron. Engng* **141**, No. 9, 04015040.

Craig, W. H. & Chua, K. (1990). Deep penetration of spud-can foundations on sand and clay. *Géotechnique* **40**, No. 4, 541–556, http://dx.doi.org/10.1680/geot.1990.40.4.541.

Dier, A., Carroll, B. & Abolfathi, S. (2004). *Guidelines for jack-up rigs with particular reference to foundation integrity*, Research report 289. Bootle, UK: Health and Safety Executive (HSE).

Dutt, R. N. & Ingram, W. B. (1984). Jackup rig siting in calcareous soils. *Proceedings of the offshore technology conference*, Houston, TX, USA, paper OTC 4840, pp. 541–548.

Hanna, A. M. & Meyerhof, G. G. (1980). Design charts for ultimate bearing capacity of foundations on sand overlying soft clay. *Can. Geotech. J.* **17**, No. 2, 300–303.

Hossain, M. S. (2014). Experimental investigation of spudcan penetration in multi-layer clays with interbedded sand layers. *Géotechnique* **64**, No. 4, 258–276, http://dx.doi.org/10.1680/geot.12.P.194.

Hossain, M. S. & Randolph, M. F. (2009). New mechanism based design approach for spudcan foundations on single layer clay. *J. Geotech. Geoenviron. Engng, ASCE* **135**, No. 9, 1264–1274.

Hossain, M. S., Hu, Y., Randolph, M. F. & White, D. J. (2005). Limiting cavity depth for spudcan foundations penetrating clay. *Géotechnique* **55**, No. 9, 679–690, http://dx.doi.org/10.1680/geot.2005.55.9.679.

Hossain, M. S., Randolph, M. F. & Saunier, Y. N. (2011). Spudcan deep penetration in multi-layered fine-grained soils. *Int. J. Phys. Modelling Geotech.* **11**, No. 3, 100–115.

Houlsby, G. T. & Martin, C. M. (2003). Undrained bearing capacity factors for conical footings on clay. *Géotechnique* **53**, No. 5, 513–520, http://dx.doi.org/10.1680/geot.2003.53.5.513.

Hu, P., Stanier, S. A., Cassidy, M. J. & Wang, D. (2014a). Predicting peak resistance of spudcan penetrating sand overlying clay. *J. Geotech. Geoenviron. Engng* **140**, No. 2, 04013009.

Hu, P., Wang, D., Cassidy, M. J. & Stanier, S. A. (2014b). Predicting the resistance profile of a spudcan penetrating sand overlying clay. *Can. Geotech. J.* **51**, No. 10, 1151–1164.

Hu, P., Stanier, S. A., Wang, D. & Cassidy, M. J. (2015). A comparison of full profile prediction methods for a spudcan penetrating sand overlying clay. *Géotechnique Lett.* **5**, No. 3, 131–139.

ISO (International Organization for Standardization) (2012). ISO 19905-1: Petroleum and natural gas industries – site specific assessment of mobile offshore units – part 1: Jack-ups. Geneva, Switzerland: ISO.

Ladd, C. C., Foot, R., Ishihara, K., Poulos, H. G. & Schlosser, F. (1977). Stress-deformation and strength characteristics. *Proceedings of the 9th international conference on soil mechanics and foundation engineering (ICSMFE)*, Tokyo, Japan, vol. 2, pp. 421–494.

Lee, K. K., Cassidy, M. J. & Randolph, M. F. (2012). Use of epoxy in developing miniature ball penetrometers. *Int. J. Phys. Modelling Geotech.* **12**, No. 3, 119–128.

Lee, K. K., Cassidy, M. J. & Randolph, M. F. (2013a). Bearing capacity on sand overlying clay soils: experimental and finite-element investigation of potential punch-through failure. *Géotechnique* **63**, No. 15, 1271–1284, http://dx.doi.org/10.1680/geot.12.P.175.

Lee, K. K., Randolph, M. F. & Cassidy, M. J. (2013b). Bearing capacity on sand overlying clay soils: a simplified conceptual model. *Géotechnique* **63**, No. 15, 1285–1297, http://dx.doi.org/10.1680/geot.12.P.176.

Lunne, T., Robertson, P. K. & Powell, J. M. (1997). *Cone penetration testing in geotechnical practice*. London, UK: Blackie Academic and Professional.

McMahon, B. T., Haigh, S. K. & Bolton, M. D. (2013). Optimal displacement mechanisms beneath shallow foundations on linear-elastic perfectly plastic soil. *Géotechnique* **63**, No. 16, 1447–1450, http://dx.doi.org/10.1680/geot.13.T.002.

Meyerhof, G. G. & Chaplin, T. K. (1953). The compression and bearing capacity of cohesive layers. *Br. J. Appl. Phys.* **4**, No. 1, 20–26.

SNAME (Society of Naval Architects and Marine Engineers) (2008). *Recommended practice for site specific assessment of mobile jack-up units*, 1st edn, T & R Bulletin 5-5A, rev 3. Alexandria, VA, USA: Society of Naval Architects and Marine Engineers.

Stanier, S. A. & White, D. J. (2013). Improved image-based deformation measurement in the centrifuge environment. *Geotech. Testing J.* **36**, No. 6, 1–14.

Stanier, S. A., Ragni, R., Bienen, B. & Cassidy, M. J. (2014). Observing the effects of sustained loading on spudcan footings in clay. *Géotechnique* **64**, No. 11, 918–926, http://dx.doi.org/10.1680/geot.14.P.003.

Stewart, D. P., Boyle, R. S. & Randolph, M. F. (1998). Experience with a new drum centrifuge. *Proceedings of the international conference on centrifuge 1998*, Tokyo, Japan, vol. 1, pp. 35–40.

Teh, K. L. (2007). *Punch-through of spudcan foundation on sand overlying clay*. PhD thesis, National University of Singapore, Singapore.

Teh, K. L., Cassidy, M. J., Leung, C. F., Chow, Y. K., Randolph, M. F. & Quah, C. K. (2008). Revealing the bearing capacity mechanisms of a penetrating spudcan through sand overlying clay. *Géotechnique* **58**, No. 10, 793–804, http://dx.doi.org/10.1680/geot.2008.58.10.793.

Teh, K. L., Leung, C. F., Chow, Y. K. & Handidjaja, P. (2009). Prediction of punch-through for spudcan penetration in sand overlying clay. *Proceedings of the offshore technology conference*, Houston, TX, USA, paper OTC 20060, pp. 1–14.

Teh, K. L., Leung, C. F., Chow, Y. K. & Cassidy, M. J. (2010). Centrifuge model study of spudcan penetration in sand overlying clay. *Géotechnique* **60**, No. 11, 825–842, http://dx.doi.org/10.1680/geot.8.P.077.

Ullah, S. N., Hu, Y., Stanier, S. A. & White, D. J. (2014). LDFE study of bottom boundary effect in foundation model tests. *Int. J. Phys. Modelling Geotech.* **14**, No. 3, 80–87.

Ullah, S. N., Stanier, S. A., Hu, Y. & White, D. J. (2016a). Foundation punch-through in clay with sand: analytical modelling. *Géotechnique*, http://dx.doi.org/10.1680/jgeot.16.P.101.

Ullah, S. N., Hu, Y., Stanier, S. A. & White, D. J. (2016b). Lateral boundary effects in centrifuge foundation tests. *Int. J. Phys. Modelling Geotech.*, http://dx.doi.org/10.1680/jphmg.15.00034.

White, D. J., Take, W. A. & Bolton, M. D. (2003). Soil deformation measurement using particle image velocimetry (PIV) and photogrammetry. *Géotechnique* **53**, No. 7, 619–631, http://dx.doi.org/10.1680/geot.2003.53.7.619.

Xu, X. (2007) *Investigation of the end bearing performance of displacement piles in sand*. PhD thesis, University of Western Australia, Perth, WA, Australia.

Young, A., Remmes, B. & Meyer, B. (1984). Foundation performance of offshore jack-up drilling rigs. *J. Geotech. Engng* **110**, No. 7, 841–859.